An Automated and Lightweight Framework for Electrolyte Diagnostics using Quantitative Microelectrode Voltammetry

Alexis M. Fenton Jr.,[a] Bertrand J. Neyhouse,[a] Kevin M. Tenny,[a]
Yet-Ming Chiang,[b] and Fikile R. Brushett[a,*]

[a] *Department of Chemical Engineering, Massachusetts Institute of Technology, Cambridge, MA 02139*
[b] *Department of Materials Science and Engineering, Massachusetts Institute of Technology, Cambridge, MA 02139*
** Corresponding author: brushett@mit.edu*

Abstract

Voltammetry is a ubiquitous electroanalytical method that can be used to help probe sustainable electrochemical technologies. When conducted with a microelectrode (radius *ca*. μm), voltammetry enables special interrogation of electrolyte solutions by minimizing distortions and facilitating near-steady-state measurements. Methodologies aimed to evaluate the behavior of redox-active species often leverage well-established, physically-grounded expressions that can be extended to examine electrolyte solutions under non-ideal conditions (e.g., signal convolution from multiple redox events) by simulating the entire voltammogram. To characterize these analyte systems, we first develop closed-form expressions—building on previous work that utilizes oblate spheroidal coordinates—and establish a framework for rapidly evaluating electrolyte composition. We subsequently apply finite difference transient voltammogram models to assess the performance of this workflow. We then validate our findings using model, deterministically-prepared nonaqueous electrolyte solutions containing *N*-[2-(methoxyethoxy)ethyl]phenothiazine, finding the toolkit is particularly adept at rapidly (< 1 min) estimating the degree to which an electrolyte solution is charged (its "state-of-charge") and remains intact (its "state-of-health"). Finally, we highlight potential extensions of this method towards advancing *in situ* or *operando* diagnostic methods within operating electrochemical devices.

Keywords: *microelectrode voltammetry, simulation, in-situ diagnostics, feature estimation, state-of-charge, state-of-health*

1. Introduction

Voltammetry is a foundational analytical method widely used to qualitatively and quantitatively characterize electrode processes in electrochemical science and engineering.[1–10] In most common applications, known physical relationships based on reaction-transport processes are used to discern key physical (thermodynamic, kinetic, and transport) properties of dissolved analytes at dilute concentrations.[1,2,11] Knowledge of these descriptors can, in turn, offer insight into (electro)chemical phenomena under more complex conditions, such as the individual species concentrations in multi-component electrolytes and/or degradation rates of unstable intermediates.[9,12] Accordingly, significant effort has been devoted to modeling voltammetric responses, and voltammograms in dilute electrolytes may be numerically, semi-analytically, and analytically simulated in multiple programming languages (e.g., C++, MATLAB®) as well as in commercial or open-source software packages (e.g., KISSA-1D©, COMSOL®, EC-Lab®).[11,13–25]

Broadly, voltammetric methods polarize a working electrode to observe reaction kinetics at the surface and reactant fluxes to the surface that manifest as current, providing mechanistic insight into electrochemical and chemical processes.[26–30] A key differentiating factor in this electrochemical response is the radius of the working electrode—macroelectrodes describe radii that are *ca*. 1–5 mm whereas microelectrodes describe radii that are *ca*. 5–50 μm. The microelectrode radius is shorter than the linear boundary layer thickness, meaning reactant can readily approach the electrode from the sides—or non-axial direction—to enable radial, diffusion-dominant steady-state concentration gradients and currents that are distinct from the linear and transient gradients engendered by larger electrodes.[1,11] These different modes of mass transport can also be formulated using a process time scale argument; for macroelectrodes, the typical experiment duration (*ca*. 200 s) is shorter than the steady-state time scale (*ca*. 2000 s)—defined as

the approximate time for the boundary layer to expand the length of one electrode radius—whereas for microelectrodes, the opposite is true (steady-state time scale *ca*. 0.01 s).[1] The smaller working electrode radius also presents unique opportunities for microelectrode voltammetry. For example, currents are on the order of nA, resulting in negligible ohmic (*iR*) potential distortions; the smaller electrode radius also results in small capacitive charging currents.[3,28] Importantly, when a microelectrode is sufficiently polarized, the steady-state reactant fluxes to the electrode surface lead to separate oxidative and reductive steady-state current plateaus.[1] These features make microelectrode voltammetry an especially powerful electroanalytical method provided environmental disturbances are minimized (e.g., vibrations) and undesired electrode processes (e.g., fouling) are controlled.[9,31]

Prior works have leveraged these attractive features of microelectrode voltammetry to successfully describe the thermodynamic, kinetic, and mass transport features of redox-active analytes.[1,14,32,33] Beyond these foundational and fundamental investigations, the limiting current behavior of microelectrode voltammetry—which may be analytically expressed for several electrode geometries (e.g., hemispherical and disk electrodes[1,34])—can be used to estimate concentrations of reacting species within an electrolyte solution.[9,12] Of note, disk microelectrodes and microfabricated electrode arrays have been used to capture the time evolution of energy storage systems where analytes are deployed at higher concentrations (e.g., 0.5 M) and/or at various oxidation states. Often, measurements estimate the state-of-charge (SOC) and state-of-health (SOH)—respectively defined as the degree of system oxidation and the ratio of the current total species concentration to its initial value—to evaluate the operational state of the electrochemical system.[9,12,31,35–39] These approaches are often accurate and can provide considerable utility,[9,12,38] though there are circumstances where limiting current plateaus do not

provide enough information to sufficiently evaluate voltammograms. For example, signal convolution from multiple redox-active species (including species that exhibit multiple sequential electron transfers)[5,30,40,41] may frustrate such analyses, along with voltammograms that do not have fully developed plateau currents—specifically, voltammograms whose cutoff or turnaround potentials are close enough to the formal redox potential that no clear plateau is observed (e.g., to avoid electrode or electrolyte solution degradation at extreme potentials).[1,31] More generally, by only considering plateau currents, the remainder of the voltammogram, which offers insights into reaction kinetics and thermodynamics, is ignored. Accordingly, analytical and numerical models have been developed that offer more comprehensive descriptions of microelectrode voltammograms, enabling the estimation of thermodynamic, kinetic, and transport parameters.[14,21,32]

While previously-developed reaction-transport models can accurately capture the electrochemical response of microelectrodes across the full range of potentials, they are often complex as compared to macroelectrode voltammetry models.[1,11] This, in turn, may contribute to their less frequent use within the broader experimental community, despite the otherwise attractive capabilities of microelectrode voltammetry.[1,9,12] One approach to potentially increase the utilization of microelectrodes within experimental applications is to develop facile and rapid algorithms that can yield features of interest within electrochemical devices, such as SOC, SOH, and degradation rates.

Here, we build on prior work to demonstrate that closed-form models can rapidly and accurately estimate features of interest in electrochemical solutions using microelectrode voltammograms. We first present frameworks to derive closed-form expressions and numerical simulators using oblate spheroidal coordinates for multiple mechanisms of electron transfer when

diffusion is the dominant mode of transport. We subsequently use the resulting steady-state expressions to estimate underlying fundamental parameters (e.g., formal redox potential, diffusion coefficients)—along with operational characteristics (e.g., SOC, SOH)—using least squares fitting. This methodology enables quantitative modeling and evaluation of electrolyte solution behavior under conditions with unknown and/or evolving analyte compositions, as might be expected within electrochemical technologies (e.g., rechargeable batteries). By developing these modeling and regression frameworks, the diagnostic capabilities of microelectrode voltammetry may be expanded to characterize complex (e.g., multicomponent) electrolyte solutions accurately, in an automated fashion, and in near-real time.

2. Methods

2.1. Theorical framework

This section presents derivations of the steady-state microelectrode models. The development of this modeling approach has a rich history in electroanalytical chemistry,[23,42,43] which we leverage to arrive at the steady-state expressions that underlie our feature estimation algorithms. Of note, we provide two approaches to derive a closed-form expression for the steady-state current at a disk microelectrode, which we refer to as the concentration-explicit method and the flux-explicit method. We first present the advantages of the oblate spheroidal coordinate system when modeling disk microelectrode behavior.

2.1.1. Model formulation in cylindrical and oblate spheroidal coordinates

Disk microelectrode models often contemplate a single-electron-transfer half-reaction posed in cylindrical coordinates.[11,44,45]

$$R \rightleftharpoons O + \mathrm{e}^- \tag{1}$$

In **Equation (1)**, R is the reduced species, O is the oxidized species, and e^- represents a single electron. Depending on the redox couple identity, the electron transfer can either be diffusively limited ("electrochemically reversible"), kinetically limited ("electrochemically irreversible"), or dependent on both ("electrochemically quasireversible"). For an electrochemically reversible redox couple, the mass conservation relation (**Equation (2)**), along with the corresponding boundary conditions (**Equations (3)**–**(7)**), can be expressed as:

$$\frac{\partial C_j}{\partial t} = D_j \nabla^2 C_j = D_j \left(\frac{\partial^2 C_j}{\partial r^2} + \frac{1}{r} \frac{\partial C_j}{\partial r} + \frac{\partial^2 C_j}{\partial z^2} \right) \tag{2}$$

$$C_j \left(r \to \infty, z \right) = C_j \left(r, z \to \infty \right) = C_{j,\infty} \tag{3}$$

$$\left(\frac{\partial C_j}{\partial r} \right) \Bigg|_{r=0} = 0 \tag{4}$$

$$\left(\frac{\partial C_R \left(r \le r_\mathrm{e}, z \right)}{\partial z} \right) \Bigg|_{z=0} + d_O \left(\frac{\partial C_O \left(r \le r_\mathrm{e}, z \right)}{\partial z} \right) \Bigg|_{z=0} = 0 \tag{5}$$

$$C_R \left(r \le r_\mathrm{e}, z \right) \Big|_{z=0} = C_O \left(r \le r_\mathrm{e}, z \right) \Big|_{z=0} \exp \left(\frac{-F\varphi}{R_\mathrm{G} T} \right) \tag{6}$$

$$\left(\frac{\partial C_j \left(r > r_\mathrm{e}, z \right)}{\partial z} \right) \Bigg|_{z=0} = 0 \tag{7}$$

Equations (3)–**(7)** are expressed in cylindrical coordinates, where j (–) represents either species R, O, or S (*vide infra*); C_j (mol m^{-3}) is the concentration of species j; t (s) is the time; r (m) is the radial spatial coordinate and z (m) is the axial spatial coordinate; D_j (m^2 s^{-1}) is the diffusion coefficient of species j; $C_{j,\infty}$ (mol m^{-3}) is the bulk/initial concentration of species j;

r_e (m) is the radius of the working electrode; d_j (–) is the ratio of diffusion coefficients $D_j D_R^{-1}$; $\varphi = E - E_0$ (V) is the overpotential, where E (V vs. a reference redox event) is the applied potential and E_0 (V vs. a reference redox event) is the formal redox potential of **Equation (1)**; R_G (8.314 J mol^{-1} K^{-1}) is the universal gas constant; T (K) is the absolute temperature; and F (96485 C mol^{-1}) is the Faraday constant. Note that **Equation (6)** is an idealized representation of the Nernst equation; concentrations are used in the place of activities, and the formal redox potential is used in the place of the standard redox potential.

Mathematical treatment of **Equations (2)**–**(7)** can be challenging due to the piecewise boundary conditions in **Equations (5)**–**(7)** (illustrated in **Figure 1a**); the separate nature of the electrochemically active and electrochemically inactive surfaces leads to singularities at the perimeter of the electrode ($(r,z) = (r_e, 0)$) which is inconvenient for analytical[14] or numerical[11] approaches. This issue may be avoided by shifting to the oblate spheroidal coordinate system, which parameterizes the ξ (−) and η (−) coordinates and are converted to *r* and *z* coordinates *via* the following relationships.[46]

$$z = r_e \xi \eta \tag{8}$$

$$r = r_e \sqrt{\left(1 + \xi^2\right)\left(1 - \eta^2\right)} \tag{9}$$

Oblate spheroidal coordinates are particularly useful for disk-type microelectrodes, as the boundary conditions are no longer piecewise—facilitating solvability—as illustrated in **Figure 1b**.

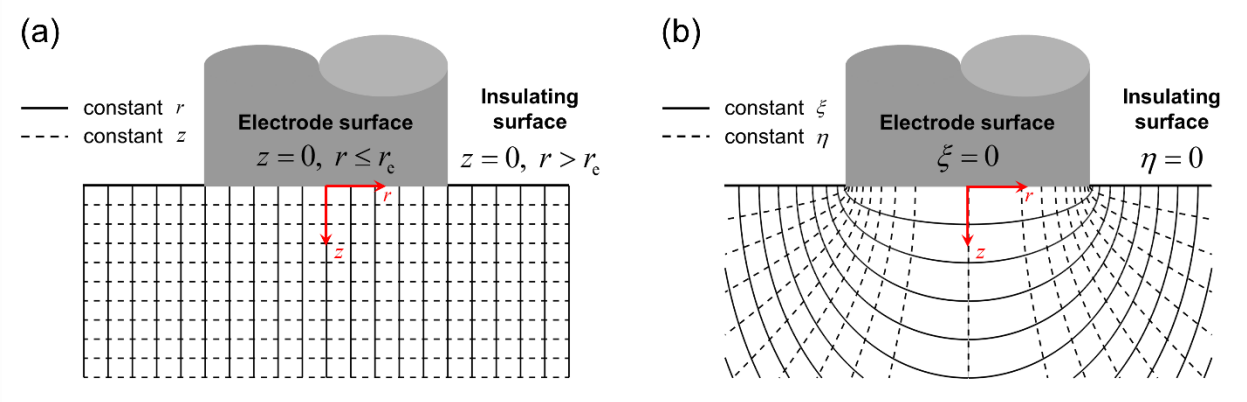

Figure 1. Modeling domain of a microelectrode in (a) cylindrical coordinates, parameterized in (r, z), and (b) oblate spheroidal coordinates, parameterized in (ξ, η).

This coordinate transform was pioneered in the field of electrochemical engineering by Professor John Newman, whose early work provided an analytical solution for the potential field extending from a rotating disk electrode.[46] This approach has since been expanded to microelectrodes, unlocking analytical expressions for steady-state voltammograms of electrochemically reversible redox couples;[42] transient voltammograms can also be simulated using numerical methods[18,43] and analytical Laplace transforms.[7] Indeed, implementing the oblate spheroidal coordinate system, in place of a cylindrical coordinate system, can often simplify electron transfer model derivations,[42,47] expanding the utility and improving the portability of microelectrode voltammogram models.

While steady-state and transient voltammetry models can solve the forward problem—that is, simulating a voltammogram given a set of parameters—they may also be used to solve the inverse problem (e.g., estimating parameter sets from voltammograms), which, in turn, can be used to estimate the identities and concentrations of analytes in an electrolyte solution *via* automated algorithms.[19] Closed-form expressions are readily adoptable for this purpose, as they can be computed nearly instantaneously and can be derived with relative ease using appropriate

coordinate systems. Though models that simulate transience are more difficult to employ for solving the inverse problem (i.e., longer simulation times), oblate spheroidal coordinates still overcome the singularity at the electrode perimeter and thus remain an attractive option for numerical methods.[18,21,43,48]

2.1.2. Single electron transfer

We first present our derivation framework by directly solving the concentration profile—the concentration-explicit approach—for an electrochemically reversible single electron transfer according to **Equation (1)** (i.e., $R \rightleftharpoons O + \mathrm{e}^-$). The full transient system—including the conservation equation, boundary conditions, and initial conditions—can be expressed in **Equations (10)**–**(14)** using transformations previously described in literature.[11,43]

$$\frac{\partial c_j}{\partial \tau} = r_\mathrm{e}^2 d_j \left(\nabla^2 c_j\right) = \frac{d_j}{\left(\xi^2+\eta^2\right)}\left\{\frac{\partial}{\partial \xi}\left[\left(1+\xi^2\right)\frac{\partial c_j}{\partial \xi}\right] + \frac{\partial}{\partial \eta}\left[\left(1-\eta^2\right)\frac{\partial c_j}{\partial \eta}\right]\right\} \tag{10}$$

$$c_j\left(\xi,\eta,\tau=0\right) = c_j(\xi\to\infty,\eta,\tau) = c_{j,\infty} \tag{11}$$

$$\left.\frac{\partial c_R}{\partial \xi}\right|_{\xi=0} + d_O \left.\frac{\partial c_O}{\partial \xi}\right|_{\xi=0} = 0 \tag{12}$$

$$\left.\frac{\partial c_j}{\partial \eta}\right|_{\eta=0} = \left.\frac{\partial c_j}{\partial \eta}\right|_{\eta=1} = 0 \tag{13}$$

$$c_R\left(\xi=0,\eta,\tau\right) = c_O\left(\xi=0,\eta,\tau\right)\exp\left(\frac{-F\varphi}{R_\mathrm{G}T}\right) \tag{14}$$

In **Equations (10)**–**(14)**, $\tau = tD_R r_\mathrm{e}^{-2}$ (–) is the dimensionless time; c_j (–) is the dimensionless concentration of species j normalized by $C_{\mathrm{total},\infty}$ (mol m^{-3}), the total bulk concentration of all species—namely, $C_{\mathrm{total},\infty} = C_{R,\infty} + C_{O,\infty}$ or $C_{\mathrm{total},\infty} = C_{R,\infty} + C_{S,\infty} + C_{O,\infty}$ (*vide infra*)—and $c_{j,\infty}$ (–) is

the dimensionless bulk/initial concentration of species j. The steady-state system of equations, with the same boundary conditions and no initial conditions, reduces to **Equation (15)**.

$$0=\left\{\frac{\partial}{\partial\xi}\left[\left(1+\xi^2\right)\frac{\partial c_j}{\partial\xi}\right]+\frac{\partial}{\partial\eta}\left[\left(1-\eta^2\right)\frac{\partial c_j}{\partial\eta}\right]\right\} \tag{15}$$

This equation may be analytically solved using a separation of variables approach, where $c_j\left(\xi,\eta\right)=Q\left(\xi\right)P\left(\eta\right)$; $Q\left(\xi\right)$ is only a function of ξ, while $P\left(\eta\right)$ is only a function of η.

$$\frac{d}{d\eta}\left[\left(1-\eta^2\right)\frac{d\left(P\left(\eta\right)\right)}{d\eta}\right]+l\left(l+1\right)P\left(\eta\right)=0 \tag{16}$$

$$\frac{d}{d\xi}\left[\left(1+\xi^2\right)\frac{d\left(Q\left(\xi\right)\right)}{d\xi}\right]-l\left(l+1\right)Q\left(\xi\right)=0 \tag{17}$$

In **Equations (16)** and **(17)**, l is a variable that is typically a whole number (i.e., $l=0,\ 1,\ 2,\ ...$) whose value is dictated by the boundary conditions. **Equation (16)** is Legendre's equation. For the no-flux boundary conditions to hold at $\eta=0$ and $\eta=1$, l must be zero; consequently, the solution for **Equation (16)** is $P\left(\eta\right)=1$. It must also hold true that $l=0$ for **Equation (17)**; this leads to the general solution of $Q\left(\xi\right)=a_1\tan^{-1}\left(\xi\right)+a_2$, where a_1 and a_2 are generic constants of integration. As such, the general solution to **Equation (15)** is expressed in **Equation (18)**.

$$\begin{aligned}c_R(\xi,\eta)&=b_1\tan^{-1}\left(\xi\right)+b_2\\ c_O(\xi,\eta)&=b_3\tan^{-1}\left(\xi\right)+b_4\end{aligned} \tag{18}$$

The relevant boundary conditions can be applied to solve for the constants of integration $b_i,\ i\in\{1,2,3,4\}$. The resulting expression, in turn, can be differentiated and incorporated into the general expression for the steady-state current (**Equation (19)**) to solve for the current of an electrochemically reversible single electron transfer (**Equation (20)**).

$$I(\varphi) = -2\pi F D_O C_{\text{total},\infty} r_e \left. \frac{dc_O}{d\xi}(\varphi) \right|_{\xi=0} \tag{19}$$

$$I(\varphi) = 4F D_O C_{\text{total},\infty} r_e \left(\frac{f_R \exp\left(\frac{F\varphi}{R_G T}\right) - f_O}{1 + d_O \exp\left(\frac{F\varphi}{R_G T}\right)} \right) \tag{20}$$

In **Equation (20)**, I (A) is the current and f_j (–) is the fraction of species j in the bulk. Note that in this work, oxidative and reductive processes are defined to have positive and negative currents, respectively. Also note that f_R and f_O are constrained according to **Equations (21)** and **(22)**:

$$f_R + f_O = 1 \tag{21}$$

$$f_O = \frac{C_{O,\infty}}{C_{\text{total},\infty}} \tag{22}$$

Equation (20) is the analytical steady-state solution used to evaluate the correctness of the overall algorithm for a single electron transfer. We note that an analogous expression can be derived for electrochemically quasireversible electron transfers, but this equation is inexact[44] and as such will not be discussed in greater detail herein.

Equation (20) can also be derived using the flux-explicit approach, which formulates the current as a function of a mass transfer coefficient and the difference in bulk and surface concentrations.[45]

$$\frac{I(\varphi)}{FA_e} = m_T C_{\text{total},\infty} \left(f_R - c_R(\xi = 0, \eta, \varphi) \right) \tag{23}$$

In **Equation (23)**, $A_e = \pi r_e^2$ (m^2) is the surface area of the microelectrode, and $m_T = \frac{4D_R}{\pi r_e}$ (m s^{-1}) is the mass transfer coefficient;[45] note the units on both sides of **Equation (23)** are those of flux (mol m^{-2} s^{-1}). Building on **Equation (12)**,

$$\frac{f_R - c_R\left(\xi = 0, \eta, \varphi\right)}{\delta_{BL}} + d_O\left(\frac{f_O - c_O\left(\xi = 0, \eta, \varphi\right)}{\delta_{BL}}\right) = 0 \tag{24}$$

Where δ_{BL} (–) is the dimensionless boundary layer thickness. When **Equation (24)** is combined with **Equation (14)**,

$$f_R + d_O f_O = c_R\left(\xi = 0, \eta, \varphi\right)\left(1 + d_O \exp\left(\frac{F\varphi}{R_G T}\right)\right) \tag{25}$$

leading to

$$c_R\left(\xi = 0, \eta, \varphi\right) = \frac{f_R + d_O f_O}{1 + d_O \exp\left(\frac{F\varphi}{R_G T}\right)} \tag{26}$$

Substituting **Equation (26)** into **Equation (23)** and performing algebraic manipulations results in

$$I\left(\varphi\right) = 4FD_O C_{\text{total},\infty} r_e \left(\frac{f_R \exp\left(\frac{F\varphi}{R_G T}\right) - f_O}{1 + d_O \exp\left(\frac{F\varphi}{R_G T}\right)}\right) \tag{27}$$

which is exactly the same as **Equation (20)**. This finding is important, as it illustrates the expression for current can be derived without direct knowledge of the complete spatial concentration profiles. Indeed, in this instance, only the concentration profiles on the surface and in the bulk solution (i.e., the regime unaffected by polarization) are required. As such, we believe the flux-explicit approach provides utility in deriving the current at a microelectrode (*vide infra*).

2.1.3. Sequential electron transfers

Stable compounds able to donate electrons sequentially are attractive as charge-carrying species in electrochemical energy storage devices, given their increased theoretical charge storage capacity per unit mass.[5,30,41] As such, the same flux-explicit approach can be invoked to solve for a sequential electron transfer mechanism, expressed in **Equation (28)**.

$$R \rightleftharpoons S + \mathrm{e}^- \rightleftharpoons O + \mathrm{e}^- \tag{28}$$

Here, S refers to the semi-oxidized (or semi-reduced) species. Note that only two sequential, electrochemically reversible electron transfers are considered. The bulk composition is assumed to be at equilibrium—that is, comproportionation/disproportionation occurs much more quickly (*ca*. 5-50 μs)[49] than the heterogeneous electrode reaction (*ca*. 0.01-100 s).[1] The boundary conditions, in turn, are analogous to those posed for the single electron transfer; specifically, **Equations (10)**, **(11)**, and **(13)** remain the same. **Equation (12)** is modified as follows to enforce net zero species flux:

$$\left.\frac{\partial c_R}{\partial \xi}\right|_{\xi=0} + d_S \left.\frac{\partial c_S}{\partial \xi}\right|_{\xi=0} + d_O \left.\frac{\partial c_O}{\partial \xi}\right|_{\xi=0} = 0 \tag{29}$$

Further, **Equation (14)** is expanded to account for the two Nernstian conditions present in the three-component system.

$$c_R\left(\xi = 0, \eta, \tau\right) = c_S\left(\xi = 0, \eta, \tau\right) \exp\left(\frac{-F\varphi_1}{R_\mathrm{G}T}\right) \tag{30}$$

$$c_S\left(\xi = 0, \eta, \tau\right) = c_O\left(\xi = 0, \eta, \tau\right) \exp\left(\frac{-F\varphi_2}{R_\mathrm{G}T}\right) \tag{31}$$

Where φ_1 (V) is the overpotential for the electron transfer $R \rightleftharpoons S + \mathrm{e}^-$; $\varphi_1 = E - E_{0,1}$, where $E_{0,1}$ (V vs. a reference redox event) is the corresponding formal redox potential. $\varphi_2 = E - E_{0,2}$ (V) is

the analog for the electron transfer $S \rightleftharpoons O + \mathrm{e}^-$, where $E_{0,2}$ (V vs. a reference redox event) is the formal redox potential for the second electron transfer.

Similar to **Equation (23)**,

$$\frac{I(\varphi_1,\varphi_2)}{FA_e} = \frac{I_1(\varphi_1,\varphi_2)+I_2(\varphi_1,\varphi_2)}{FA_e} = m_T C_{\text{total},\infty}\left\{ f_R - c_R(\xi=0,\eta,\varphi_1,\varphi_2) - d_O\left[f_O - c_O(\xi=0,\eta,\varphi_1,\varphi_2)\right]\right\} \tag{32}$$

In **Equation (32)**, I_1 (A) is the current generated by the reaction $R \rightleftharpoons S + \mathrm{e}^-$, while I_2 (A) is the current generated by the reaction $S \rightleftharpoons O + \mathrm{e}^-$. **Equations (29)**, **(30)**, and **(31)** can analogously be evaluated to yield

$$c_R(\xi=0,\eta,\varphi_1,\varphi_2) = \frac{f_R + d_S f_S + d_O f_O}{1 + d_S \exp\left(\frac{F\varphi_1}{R_G T}\right) + d_O \exp\left(\frac{F(\varphi_1+\varphi_2)}{R_G T}\right)} \tag{33}$$

$$c_O(\xi=0,\eta,\varphi_1,\varphi_2) = \frac{(f_R + d_S f_S + d_O f_O)\exp\left(\frac{F(\varphi_1+\varphi_2)}{R_G T}\right)}{1 + d_S \exp\left(\frac{F\varphi_1}{R_G T}\right) + d_O \exp\left(\frac{F(\varphi_1+\varphi_2)}{R_G T}\right)} \tag{34}$$

which, when combined with **Equation (32)**, result in the general expression

$$I(\varphi_1,\varphi_2) = \left\{ \frac{4FD_R C_{\text{total},\infty} r_e}{1 + d_S \exp\left(\frac{F\varphi_1}{R_G T}\right) + d_O \exp\left(\frac{F(\varphi_1+\varphi_2)}{R_G T}\right)} \right\} \cdot \left\{ f_R\left[d_S \exp\left(\frac{F\varphi_1}{R_G T}\right) + 2d_O \exp\left(\frac{F(\varphi_1+\varphi_2)}{R_G T}\right)\right] + f_S\left[d_S\left(d_O \exp\left(\frac{F(\varphi_1+\varphi_2)}{R_G T}\right) - 1\right)\right] + f_O\left[-d_O\left(2 + d_S \exp\left(\frac{F\varphi_1}{R_G T}\right)\right)\right]\right\} \tag{35}$$

We note that for the sequential electron transfer mechanism, f_R, f_S, and f_O are related not only by the constraints that all fractions must sum to unity and by the amount of positive charge stored

in this redox couple (respectively shown *via* **Equations (21)** and **(22)** for a single electron transfer) but also by the approximate equilibrium arising from rapid comproportionation/disproportionation.[49] As a result, the constraints on the three fractions are described in **Equations (36)**–**(38)**, leading to a unique set of species fractions given a particular degree of system oxidation, along with both formal redox potentials.

$$f_R + f_S + f_O = 1 \tag{36}$$

$$\left(\frac{f_S + 2f_O}{2}\right) = \frac{C_{S,\infty} + 2C_{O,\infty}}{2C_{\text{total},\infty}} \tag{37}$$

$$\frac{f_S^2}{f_R f_O} = \exp\left(\frac{F\left(E_{0,2} - E_{0,1}\right)}{R_G T}\right) \tag{38}$$

As an initial validation, **Equation (35)** reduces to Equation (137) from Ref 45 when only oxidized species are present in the bulk, when all diffusion coefficients are equal, and when the current polarity is reversed (cathodic currents are positive in that reference). It is also possible to derive **Equation (35)** using the concentration-explicit method, but the concentration profiles themselves are not accurate; indeed, the monotonic concentration profiles derived in **Section 2.1.2** cannot capture the non-monotonic behavior the semi-oxidized intermediate may exhibit.[20,45]

2.2. Computational methods

Most simulations were run on MATLAB® R2020a using an Intel® Core™ i7-7500U CPU @ 2.70 GHz 2.90 GHz (16 GB RAM) laptop computer. The generation of synthetic data for evaluating the accuracy of parameters (*vide infra*) was performed on MATLAB® R2019b using an Intel® Xeon® CPU E5-2687W 0 @ 3.10 GHz 3.10 GHz (128 GB RAM) workstation computer. The closed-form expressions were evaluated almost instantaneously—on average *ca*. 1 ms for a

single electron transfer and on average < 40 ms for sequential electron transfers. Further, our model validations are summarized using a checklist recently developed for theoretical battery studies (**Table S3**).[50]

Our in-house numerical scheme integrates the approaches of Compton, Laborda, and Ward[11], Myland and Oldham[18], and Qian et al.[43] by using an alternating direction implicit finite-difference simulator in oblate spheroidal coordinates to track all species concentrations. The algorithm simulates an electrochemically reversible single electron transfer using **Equations (10)**–**(14)** and models an electrochemically quasireversible single electron transfer using the Butler-Volmer formulation, in which **Equation (14)** is replaced with **Equation (39)**.

$$-\left.\frac{\partial c_R}{\partial \xi}\right|_{\xi=0} = K_0 d_O \eta \left(c_O\left(\xi=0,\eta\right)\exp\left(\frac{-\alpha_c F\varphi}{R_G T}\right) - c_R\left(\xi=0,\eta\right)\exp\left(\frac{\left(1-\alpha_c\right)F\varphi}{R_G T}\right)\right) \quad (39)$$

In **Equation (39)**, $K_0 = k_0 r_e D_O^{-1}$ (–) is the dimensionless heterogeneous rate constant—k_0 (m s^{-1}) is the dimensional analog—and α_c (–), set to 0.5, is the cathodic transfer coefficient. Electrochemically reversible sequential electron transfers are simulated based on **Equations (10)**, **(11)**, **(13)**, **(29)**, **(30)**, and **(31)**. When two sequential electrochemically quasireversible electron transfers are simulated, **Equations (30)** and **(31)** are replaced with **Equations (40)** and **(41)**.

$$-\left.\frac{\partial c_R}{\partial \xi}\right|_{\xi=0} = K_{0,1} d_O \eta \left(c_S\left(\xi=0,\eta\right)\exp\left(\frac{-\alpha_{c,1} F\varphi_1}{R_G T}\right) - c_R\left(\xi=0,\eta\right)\exp\left(\frac{\left(1-\alpha_{c,1}\right)F\varphi_1}{R_G T}\right)\right) \quad (40)$$

$$-\left.\frac{\partial c_S}{\partial \xi}\right|_{\xi=0} = K_{0,2}\left(\frac{d_O}{d_S}\right)\eta \left(c_O\left(\xi=0,\eta\right)\exp\left(\frac{-\alpha_{c,2} F\varphi_2}{R_G T}\right) - c_S\left(\xi=0,\eta\right)\exp\left(\frac{\left(1-\alpha_{c,2}\right)F\varphi_2}{R_G T}\right)\right)$$

(41)

In **Equations (40)** and **(41)**, $K_{0,q}$ and $\alpha_{c,q}$ ($q = 1, 2$) represent the dimensionless heterogeneous rate constant and cathodic transfer coefficient for the q^{th} electron transfer, respectively. The reported current for both electrode processes is evaluated by numerically integrating the concentration gradient using a trapezoidal approximation across the $\eta \in [0,1]$ domain, since the surface species concentration may not necessarily be uniform. We implement parallelization using MATLAB®'s "*parfor*" command, and minimization was performed using "*fmincon*", MATLAB®'s minimization routine that accounts for constraints (e.g., by enforcing lower and upper values to bound an estimated descriptor). The numerical simulations with 2000 time steps were evaluated in *ca*. 400 s on the laptop computer; further details on—and explicit mathematic formulations of—the finite difference framework can be found in the Supplementary Information (SI) **Section S.2**. For the sequential electron transfer model with dissimilar diffusion coefficients, current estimates from the in-house numerical simulator will differ from those of the closed-form model—all other factors equal—because comproportionation is not enforced at the interior points utilized by the finite difference algorithm. This contrasts with the closed-form models, which only reference the surface and infinite boundary conditions where comproportionation is strictly enforced. Despite this difference, we find the in-house numerical simulator is still useful in evaluating the performance of the closed-form simulator (*vide infra*).

COMSOL® Multiphysics (version 5.6) was used to assess the fidelity of the in-house finite difference simulator; as detailed below, the in-house simulator was primarily used in this work due to its facile customizability and its greater ease of comparison to the closed-form models. All COMSOL® programs were executed on the previously-mentioned laptop computer, and mesh information used to discretize and solve the electrochemical model is included in the SI (**Section S.1**). The electrochemical model utilized by COMSOL® evaluates a single electron transfer

(**Equation (1)**) using **Equations (42)**–**(44)**. For transparency, we provide the equations used by COMSOL®—as reported in the program itself and within supporting documentation; we also note similarities between the COMSOL® and in-house formulations.[51,52]

$$\frac{\partial C_i}{\partial t} + \nabla \cdot \mathbf{J}_i = R_i \tag{42}$$

$$\mathbf{J}_i = -D_i \nabla C_i \tag{43}$$

$$\phi_l = 0 \tag{44}$$

In **Equations (42)**–**(44)**, the vector $\mathbf{J}_i$ (mol m^{-2} s^{-1}) is the flux of species i, R_i (mol m^{-3} s^{-1})—here, set to 0—is the volumetric reaction rate, and ϕ_l (V) is the electrolyte potential or ohmic drop.[52] This set of equations is represented by **Equation (39)** in the in-house model.

The boundary conditions are as follows: a no-flux boundary condition (**Equation (45)**) is applied as a semi-infinite boundary condition far from the electrode; axial symmetry (i.e., no flux) is applied to the $r = 0$ axis and on the insulating surface surrounding the electrode; charged species flux is equated to the current passed (**Equation (46)**); and an electroanalytical Butler-Volmer expression (**Equation (47)**) with a cathodic transfer coefficient, also set to 0.5, is leveraged, which, in turn, was integrated across the microelectrode surface in **Equation (48)**.[51] Only reduced species is initially present.

$$-\mathbf{n} \cdot \left(\mathbf{J}_i + \mathbf{u} C_i \right) = 0 \tag{45}$$

$$-\mathbf{n} \cdot \mathbf{J}_i = \frac{\upsilon_i i_{\text{curr}}}{n_\text{e} F} \tag{46}$$

$$i_{\text{curr}} = n_\text{e} F k_0 \left(C_{R,S'} \exp\left(\frac{\left(n_\text{e} - \alpha_c \right) F \varphi}{R_\text{G} T} \right) - C_{O,S'} \exp\left(\frac{-\alpha_c F \varphi}{R_\text{G} T} \right) \right) \tag{47}$$

$$I = \int_{S'} i_{\text{curr}} dA \tag{48}$$

In **Equations (45)**–**(48)**, $\mathbf{n}$ indicates the normal vector in the radial or axial direction, $\mathbf{u}$ (m s^{-1}) is the velocity vector (here, 0), υ_i (–) is the stoichiometric coefficient implicitly present in the redox reaction within **Equation (1)** (respectively 1 and –1 for R and O within the COMSOL® module), n_e (–) is the number of electrons transferred (here, 1), i_{curr} (A m^{-2}) is the current density equal to the flux of charge to the electrode surface (represented by S'), $C_{j,S'}$ (mol m^{-3}) is the concentration of species j on S', dA is a generic areal element (m^2), and T is the absolute temperature (here, 298.15 K); **Equations (45)**–**(48)** are analogous to **Equations (12)**, **(19)**, and **(39)**. Two boundary probes (a calculation feature within COMSOL®) were applied to determine the total current (A) and electric potential (V) across the microelectrode, and the simulated technique was cyclic voltammetry. As shown in **Table S1**, a parametric sweep was conducted across nine values of k_0 for both the COMSOL® and in-house algorithms. Each simulation, in turn, involved *ca*. 200–250 time steps and took ≤ 35 s, meaning the entire parametric sweep took ≤ 10 min; nine simulations were conducted per sweep. Further details are provided in the SI (**Section S.1**).

2.3. Experimental methods and procedure

All chemicals were used as received, and all experiments were conducted in a glovebox (MBraun Labmaster, H_2O < 5 ppm, O_2 < 1 ppm) filled with argon (Airgas, purity of *ca*. 100 %, catalog number AR UHP300). The glovebox temperature was *ca.* 27 °C. All the materials were

opened and stored in the glovebox and were directly transferred from their container to a 5 mL volumetric flask with a plastic spatula to ensure the mass of material in the solution matched the balance reading (Mettler Toledo, Balance XS64, 61 g capacity with ± 0.1 mg readability). Every solution studied contained between 5–25 mM of either ferrocene (Sigma Aldrich, 98 %, F408), *N*-[2-(2-methoxyethoxy)ethyl]phenothiazine (MEEPT, Tokyo Chemical Industry Co., M3068, > 98.0 %), and/or MEEPT–tetrafluoroborate (MEEPT–BF_4)—synthesized and purified as previously described[53,54]—along with *ca*. 0.5 M tetraethylammonium tetrafluoroborate ($TEABF_4$, Gotion, > 99.9 %) in acetonitrile (Sigma-Aldrich®, 34851, ≥ 99.9 %). Ferrocene was also used as an internal standard for the reference electrode[55] in a separate solution (also containing 0.5 M $TEABF_4$ in acetonitrile) at a concentration of *ca*. 8 mM.

The working electrode was a gold disk microelectrode (Bioanalytical Systems, Inc. (BASi), 10 μm nominal dia., MF-2006)—referred to as the "microelectrode"—or a glassy carbon disk electrode (CH Instruments, 3 mm dia., CHI104) referred to as the "macroelectrode". Both were polished with 0.05 μm alumina powder (Buehler MicroPolish Powder, 4010075) in deionized water (Millipore, 18.2 MΩ cm) and dried with compressed air. Neither lens paper nor sonication was utilized in the polishing process. After polishing, care was taken to ensure the prepared electrode surfaces did not contact any materials aside from air (and in the glovebox, Ar) prior to immersion in the solution of interest. A Ag/Ag^+ electrode was prepared using a non-aqueous reference electrode kit (BASi, MF-2062) filled with *ca*. 10 mM silver tetrafluoroborate ($AgBF_4$, Aldrich®, ≥ 99.99 %, 483052) in a solution of *ca*. 0.5 M $TEABF_4$ and acetonitrile. The counter electrode was a platinum (Pt) coil electrode (BASi, 99.95 %, MW-1033). When not in use, the Ag/Ag^+ reference electrode was stored in the glovebox in a fill solution of the same composition.

Two voltammetry techniques were employed: cyclic voltammetry (CV) and cyclic square wave (CSW) voltammetry. CV was performed using both the microelectrode and macroelectrode, whereas CSW voltammetry was only performed with the macroelectrode. Generally, macroelectrode voltammograms were evaluated to estimate the true values of the parameters during experimental validation of the models (*vide infra*) and to verify the microelectrode radius—further details are found in the SI (**Sections S.4 and S.5**). All microelectrode studies were conducted using a CHI630E potentiostat (CH Instruments, Inc.) and processed using software provided by the same company ("CHI630E Electrochemical Analyzer"). All macroelectrode experiments were conducted using a VSP potentiostat (BioLogic) with EC-Lab® software; all data was processed with Microsoft Excel and MATLAB® R2020a. The potential range for all MEEPT experiments was from –0.3 V to 0.75 V vs. the Ag/Ag^+ reference redox event, while the range for ferrocene studies was from –0.3 V to 0.4 V vs. the Ag/Ag^+ reference redox event. Specifically, the most negative and initial potential was set to be *ca.* 300 mV lower than the formal redox potential of ferrocene, while the most positive (and the turnaround) potential of the voltammetric experiment was set to be *ca.* 200–300 mV higher than the formal redox potential of MEEPT or ferrocene to minimally influence the voltammogram shape[1] while avoiding solution or electrode decomposition that may occur at extreme potentials.[31]

Microelectrode voltammograms were acquired at a scan rate of 10 mV s^{-1}, with a rest time of 2 s before acquisition, a potential resolution of 1 mV, a sensitivity of 1×10^{-8} A V^{-1}, and the same potential bounds as those collected for the macroelectrode studies. Nine microelectrode voltammograms were acquired for electrolyte solutions containing MEEPT for statistical rigor, while only six were obtained for electrolyte solutions containing ferrocene to enable statistical rigor while minimizing possible electrode fouling.[56,57]

Macroelectrode cyclic voltammograms were obtained at 10, 25, 50, 100, 200, and 500 mV s^{-1}, with all voltammograms corrected for resistance-driven potential distortions using "*iR* determination with electrochemical impedance spectroscopy" (the "ZIR" protocol);[58] the working electrode potential was set to its open-circuit value, a delay of 10 % of the period duration was added before the measurement, a sinusoidal potential with a 20 mV amplitude and a 100 kHz frequency was applied, and the reported resistance was averaged over four measurements. The resistance was compensated 85 % by the software during the experiment; the remaining 15 % was not corrected post experiment, as macroelectrode cyclic voltammograms were solely used to estimate the diffusion coefficients of reduced and oxidized MEEPT, a process that only utilizes the peak current (*via* Randles-Ševčik analysis). We note the baseline currents should not be appreciably distorted, as the potential of the uncompensated peak was at least *ca*. 300 mV from the turnaround potential in all cases. We also note that the solution resistance was not fully compensated during acquisition to avoid possible oscillations in the potentiostat.[58] After each cyclic voltammogram was obtained, the electrolyte solution was manually swirled or agitated to allow the boundary layer to reset.

CSW voltammograms were obtained using the same potential bounds as those in the cyclic voltammograms. The pulse duration (per half-period) was 100 ms, the step height was 10 mV, and the pulse height was 50 mV, resulting in an effective scan rate of 50 mV s^{-1}. The potential was held at the initial, most negative (reductive) potential for 2 s before the initial positive (oxidizing) sweep, and the reported current for each potential step was determined by averaging the raw current over the last 30 % of the step. At least six CSW voltammograms were obtained at these same conditions for all solutions tested. The "ZIR" protocol was performed the same way as with

CV; further, the electrolyte solution was manually swirled or agitated to allow the boundary layer to reset.

To calibrate the applied potential to that of the ferrocene redox event and to estimate the radius of the microelectrode, a separate electrolyte solution of ferrocene was used to avoid signal convolution from either MEEPT or MEEPT–BF_4. To enable rapid transfer of the three-electrode configuration between electrolyte solutions, a separate vial containing only acetonitrile (no analyte or supporting salt) was used to rinse the electrodes. More specifically, after removing the electrodes from MEEPT- or MEEPT–BF_4-containing electrolyte solutions, they were gently dried with Kimwipes—avoiding direct contact with the working electrode surface—and then transferred to the solvent-containing vial. After residing and being intermittently swirled in the solution for 10–20 s, the electrodes were again removed, gently dried with Kimwipes, and inserted into the ferrocene-containing electrolyte solution. Though somewhat labor-intensive, this approach reduces the potential for cross-contamination, as illustrated in the SI (**Section S.6**).

3. Results and discussion

3.1. Analysis of the steady-state electrochemically reversible case

Exact closed-form expressions are powerful tools for steady-state modeling and can also serve as a sufficient proxy for transient behavior closely resembling the steady-state (*vide infra*). The rapidity with which closed-form expressions can be computed makes these models especially useful for parameter estimation routines. In particular, the analytical equations, **Equations (20)** and **(35)**, can be used to interpret the behavior of microelectrode voltammograms. The expression obtained for a steady-state electrochemically reversible electron transfer (**Equation (20)**) is validated, as it matches the expression previously derived using cylindrical coordinates.[45] Though

we have not been able to find a derivation of **Equation (35)**, the general expression reduces to an equation from the literature when imposing the appropriate constraints (specifically, equal diffusion coefficients, only oxidized species in the bulk).[45] The flux-explicit approach was also used when generating the current expression for both electron transfer mechanisms, further suggesting the correctness of **Equation (35)**. To illustrate the versatility of these general models, the expressions from **Equations (20)** and **(35)** are plotted in **Figure 2** at various SOCs and, for the sequential electron transfer mechanism, various gaps in the formal redox potential of each electron-transfer event (denoted as $\Delta E_0 = E_{0,2} - E_{0,1}$ (V)). Overall, **Figure 2** illustrates that closed-form expressions which describe the electrochemical response of a microelectrode can enable rapid simulation of different electrode processes across a wide range of conditions, in turn demonstrating its potential ability to model diverse electrode processes that may occur within electrolyte solutions.

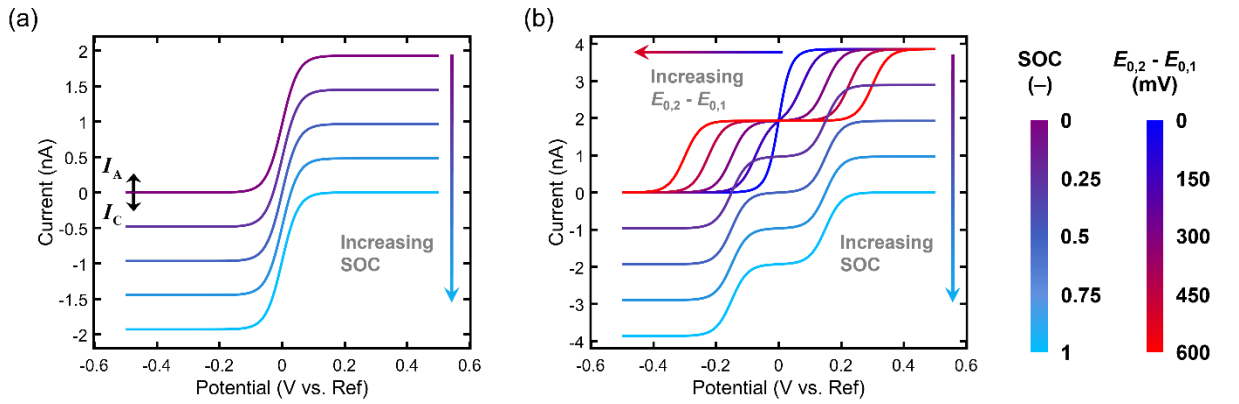

Figure 2. Plots of steady-state microelectrode voltammograms simulated using closed-form expressions for (a) an electrochemically reversible single electron transfer at various SOCs and (b) electrochemically reversible sequential electron transfers at various formal electrode potential gaps ($\Delta E_0 = E_{0,2} - E_{0,1}$) and SOCs. The average formal electrode potential $E_{0,avg} = 0.5\left(E_{0,1} + E_{0,2}\right)$ was 0 V vs. an arbitrary reference, the total concentration was 1 mM, and the diffusion coefficients for all species were set to 1×10^{-9} m^2 s^{-1}, the working electrode radius is 5 μm, and the temperature is 298.15 K. SOCs and formal redox potential gaps (the latter only applicable for (b)) are shown on the color bars on the right. The exact SOCs are (descending the color bar) 0, 0.25, 0.5, 0.75, and 1, while the exact formal electrode potential gaps are (descending) 0, 150, 300, 450, and 600 mV. Note that, by convention, a SOC of zero means that only the reduced species is present in the bulk. As shown in (a), all positive currents are oxidative (anodic), and negative currents are reductive (cathodic).

3.2. Numerical simulation of transient voltammograms *via* oblate spheroidal coordinates

While closed-form expressions for steady-state voltammograms are generally useful for electroanalysis, certain scientifically relevant scenarios (e.g., fast scan rate voltammetry, kinetically-limited electron transfers) cannot be perfectly captured, encouraging alternative simulation approaches. By introducing transience, the mass conservation equation becomes dependent on three variables (two spatial and one temporal)—as shown in **Equation (10)**—resulting in a more mathematically complex equation that, to our knowledge, has yet to be reduced to a closed-form solution (though accurate empirical approximations have been formulated).[1,45] As such, **Equation (10)** must be solved numerically, though the transformation from cylindrical coordinates to other systems (e.g., oblate spheroidal coordinates) still simplifies model

construction if the boundary conditions remain homogeneous without any singularities.[20,21] Accordingly, we generate a finite-difference numerical simulator to model transient voltammograms under a range of conditions, exemplified in **Figure 3a**, and to validate the analytical steady-state findings by simulating transient voltammograms at slow scan rates (*vide infra*).

To validate the numerical simulator constructed using oblate spheroidal coordinates, microelectrode voltammograms were generated in COMSOL® using the procedure outlined in **Section 2.2**. Specifically, the COMSOL® simulations were run at nine different heterogeneous rate constants—ranging from 1×10^{-6} to 1×10^{-2} m s^{-1}—to explore various degrees of electrochemical reversibility, from nearly irreversible to nearly reversible.[32] These results were directly compared to those from the in-house simulator modeled using the same set of parameters, visualized in **Figure 3b**.

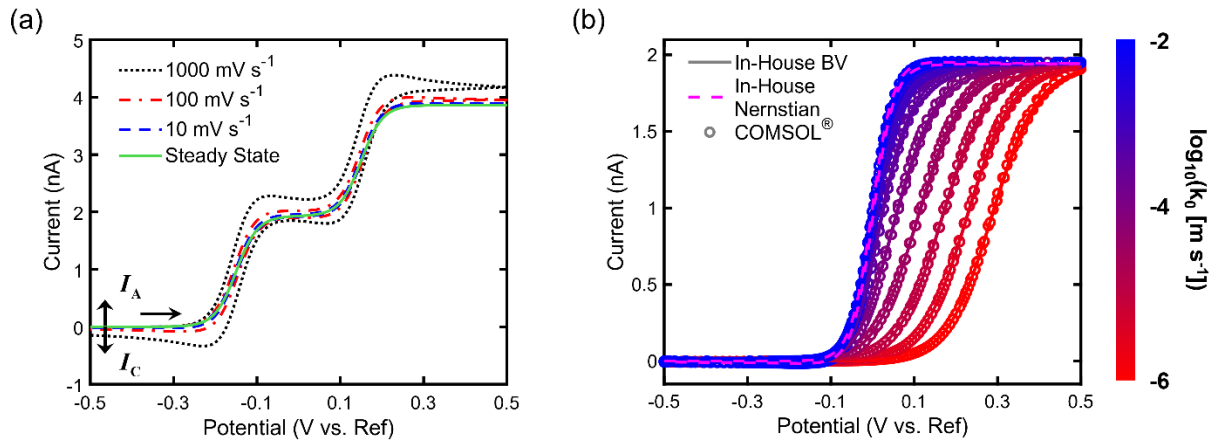

Figure 3. Transient voltammograms simulated with a finite difference numerical simulator. (a) Electrochemically reversible sequential electron transfers simulated at various scan rates, demonstrating the ability of the numerical simulator to model relevant redox mechanisms under transient conditions. (b) Validation of the numerical simulator. Butler-Volmer single electron transfers were simulated at a scan rate of 10 mV s^{-1} with increasing heterogeneous rate constant (k_0) values from 1×10^{-6} – 1×10^{-2} m s^{-1}. Exact values of k_0, descending the color bar, are $1 \times 10^{-0.5g}$ m s^{-1}, $g \in \{4,5,...,11,12\}$. In all cases, the formal redox potential is 0 V vs. an arbitrary reference, only the reduced species is in the bulk at a concentration of 1 mM, the working electrode radius is 5 μm, the diffusion coefficients of the oxidized and reduced species are both 1×10^{-9} m^2 s^{-1}, and the temperature is 298.15 K. Note the color bar only applies to panel (b). As shown in (a), all positive currents are oxidative (anodic), negative currents are reductive (cathodic), and the horizontal arrow indicates the initial sweep direction is oxidative.

The COMSOL® and in-house numerical simulation results are well-aligned, validating the in-house numerical simulator as an analytical tool—indeed, the maximum difference between the in-house and COMSOL®-simulated plateau currents at the (oxidative) turnaround potential is less than 1 %. We note that it is challenging to further evaluate the numerical values of the errors, as the number of time steps the in-house simulator uses (2000) exceeds that of the COMSOL® simulations (*ca.* 200-250), stymying direct comparison without interpolation. The in-house MATLAB® numerical model is used for the remainder of this work; since the closed form expressions are also modeled in MATLAB®, direct comparisons can be readily made between the two. Separately, simulators coded from scratch have advantages; routines built upon physical

relationships can be written in open-source languages (e.g., Python) to increase accessibility and can offer greater versatility to probe uncommon or novel mechanisms not always integrated into commercial software packages. In other instances, COMSOL® may be the preferred option, such as when simulation speed is important (i.e., *ca*. 35 s for a COMSOL® simulation compared to *ca*. 400 s for an in-house finite-difference simulation).

3.3. Detailed analysis of steady-state expressions *via* numerical simulations

The fast computation times for solving analytical expressions can enable rapid parameter estimation procedures for purposes such as predicting the identities and concentrations of analytes in electrolyte solutions.[21] Our approach to evaluate the efficacy of our single and sequential electron transfer models is inspired by a previous automated approach that evaluates electrochemical kinetics (an exercise beyond the scope of this work) using the Marquardt algorithm, in turn, motivated by the works of Oldham and Zoski and of Mirkin and Bard.[59–61] Specifically, we evaluated the accuracy of two parameter sets. One set is denoted as the "fundamental" set, which consists of the electrochemical and transport descriptors commonly evaluated in traditional electroanalysis; for the single electron transfer model, E_0, D_R, and D_O were estimated, whereas for the sequential electron transfer model, $E_{0,1}$, $E_{0,2}$, D_R, D_S, and D_O were estimated. This scenario is intended to represent a typical evaluation of a novel analyte, where the input concentration is known from electrolyte solution preparation but other parameters, such as the formal redox potential and diffusion coefficients, are unknown.

The second parameter set is denoted as the "operational" set, where E_0, the SOC, and the SOH—the latter two often used to characterize electrochemical energy storage systems—were

estimated. As mentioned in **Section 1**, the SOC represents the degree of system oxidation—**Equation (49)** for a single electron transfer and **Equation (50)** for two sequential electron transfers, respectively—while the SOH here represents the ratio of the total concentration to the maximum total concentration $C_{\text{total},\infty}^{\max}$ (mol m^{-3}) within this particular study (**Equation (51)**). E_0 was estimated because the thermodynamic formal redox potential is a function of SOC *via* the Nernst equation (**Equations (14)** and **(30)**).

$$\text{SOC} = f_O \tag{49}$$

$$\text{SOC} = \frac{f_S + 2f_O}{2} \tag{50}$$

$$\text{SOH} = \frac{C_{\text{total},\infty}}{C_{\text{total},\infty}^{\max}} \tag{51}$$

This scenario, in turn, reflects situations where fundamental descriptors are already known—perhaps from prior experiments—but the current state of the electrolyte solution (e.g., SOC and SOH) is not, as may be the case within an operating electrochemical device.

Our procedure uses least squares regression according to **Equation (52)**.

$$\boldsymbol{\theta}_{\mathbf{best}} = \arg\min_{\boldsymbol{\theta}} \left(\left\| \boldsymbol{I}_{\mathbf{obs}} - \boldsymbol{I}\left(\boldsymbol{\theta}\right) \right\|_2 \right) \tag{52}$$

In **Equation (52)**, $\boldsymbol{\theta}$ (multiple units) is a vector of unknown descriptors to be estimated. For example, $\boldsymbol{\theta}$ could be a vector of electrochemical and transport descriptors (specifically, E_0, D_R, and D_O) or operational characteristics such as the SOC or SOH. $\boldsymbol{I}_{\mathbf{obs}}$ (A) is the vector of measured currents (either experimentally or numerically generated) of the entire voltammogram, $\boldsymbol{I}\left(\boldsymbol{\theta}\right)$ (A) is the vector of modeled currents of the entire voltammogram, and $\boldsymbol{\theta}_{\mathbf{best}}$ (multiple units) is the set of descriptors that minimizes the 2-norm of the errors ($\left\| \boldsymbol{I}_{\mathbf{obs}} - \boldsymbol{I}\left(\boldsymbol{\theta}\right) \right\|_2$). By treating the input

parameters for the numerical simulator as ground truth, the predicted parameters (θ_{best}) can be compared with the known values to provide a representative estimate of how well the analytical expressions may predict relevant descriptors.

The in-house numerical simulator can be used to assess the accuracy of steady-state models, as transient voltammograms can be readily simulated at various known parameter sets while capturing the partially-transient nature of experimental data.[61] The use of simulated data can also limit confounding experimental factors that are difficult to quantify or control (e.g., imperfect working electrode polishing, spatial variations in glovebox temperature).[40] As such, the predictive ability of both the reversible single electron and sequential electron transfer models was evaluated by numerically simulating multiple voltammograms at a scan rate of 10 mV s^{-1}, a typical scan rate used in experimental microelectrode studies. Parameter sweeps were performed where one parameter was varied at a time (others were held constant), and the error in the resulting estimates were evaluated; the chosen values reflect commonly-observed conditions encountered in electrochemical studies.[9,27,62,63] For the single electron model, d_O, SOC, and SOH were varied across 11 equally-spaced values; d_O ranged between 0.5 and 2, the SOC ranged between 0 and 1, and the SOH varied between 1/11 to 1. For the sequential electron model, these same three parameters, along with ΔE_0 and d_S, were varied across 11 equally-spaced values; the ranges for d_O, SOC, and SOH were unchanged, ΔE_0 ranged between 0 and 0.4 V, and d_S ranged between 0.5 and 2. Parameter sweeps for each model took < 3 h on the aforementioned workstation computational resource.

The objective function in **Equation (52)** was minimized to estimate $\boldsymbol{\theta}_{\mathbf{best}}$. In this scenario, $\boldsymbol{I}_{\mathbf{obs}}$ is generated by the numerical simulations *a priori*, and $\boldsymbol{I}(\boldsymbol{\theta})$ is the steady-state model parameterized by $\boldsymbol{\theta}$. In addition, the initial guess for the formal electrode potential was varied across seven values—from –30 to +30 mV of the known true formal electrode potential at 10 mV intervals. As a result, for each parameter varied, 77 optimizations were performed for the study involving numerical simulations; 63 were performed when evaluating the experimental data (*vide infra*). The combined simulation time for all seven initial guesses was < 50 s for every instance on the previously described laptop computational resource, potentially enabling lightweight and near-real time analyses. Subsequently, $\boldsymbol{\theta}_{\mathbf{best}}$ was compared to the known parameter set used to generate the numerical simulation *via* the root mean squared error (RMSE), defined in **Equation (53)**.

$$\mathrm{RMSE}_i = \sqrt{\frac{1}{N_\mathrm{t}} \sum_{k=1}^{N_\mathrm{t}} \left(\left(\theta_{i,k,\mathrm{true}} - \theta_{i,k,\mathrm{guess}} \right)^2 \right)} \tag{53}$$

In **Equation (53)**, RMSE_i (varied units) is the root mean squared error of parameter i (e.g., E_0, D_O), N_t (–) is the total number of trials evaluated in the calculated value of RMSE_i (11 for synthetically-generated data, nine for experimental data), k (–) is a counter for each trial, $\theta_{i,k,\mathrm{true}}$ (varied units) is the value of the known parameter i of the k^{th} trial, and $\theta_{i,k,\mathrm{guess}}$ (varied units) is the analogue for the estimated parameter—we note the vectorized form of $\boldsymbol{\theta}_{\mathbf{k,true}}$ (multiple units) and $\boldsymbol{\theta}_{\mathbf{k,guess}}$ (multiple units) have the same parameter ordering as $\boldsymbol{\theta}$ and $\boldsymbol{\theta}_{\mathbf{best}}$. The RMSE is also the standard deviation of the residuals, and statistical analyses can be performed on RMSE values themselves—that is, an array of RMSEs can have a mean and a variance. Here, seven values of

RMSE_i (one per initial guess) were calculated for every study. The average of these seven RMSE_i values for synthetic data of a single electron transfer—with each RMSE_i encompassing the average of the squared error for all 11 trials—is plotted in **Figure 4**; the standard deviation of these errors is also reported as error bars, and the total time to evaluate all 77 optimizations for each bar (t_{sim} (s)) is less than 20 s (**Figure 4b**). Representative synthetic voltammograms and their data-model fits used within this regression process can be found in the SI (**Section S.3**).

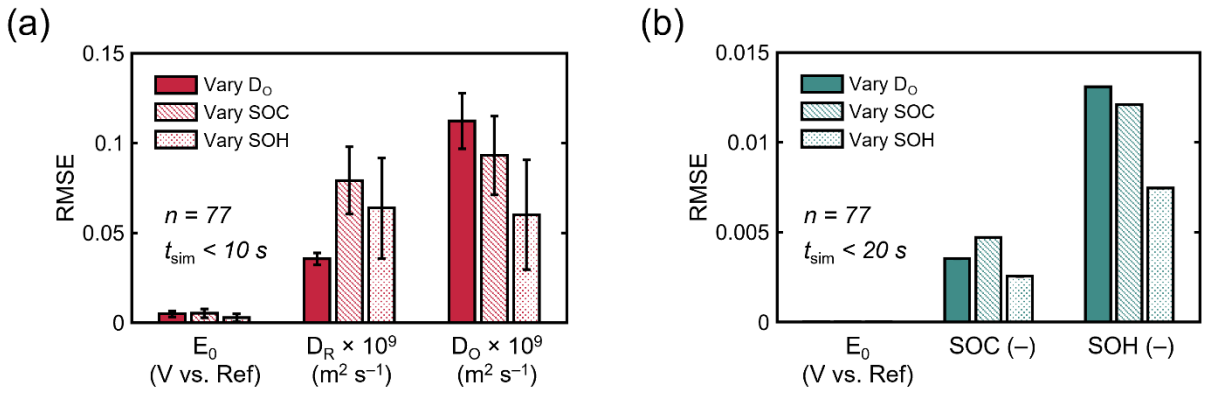

Figure 4. Error of feature estimation (n = 77 for each bar), evaluated in its entirety in less than 20 s, using the electrochemically reversible single electron transfer steady-state model. Two instances are explored. The first is (a) the "fundamental" scenario, and the second graph estimates (b) the "operational" scenario. Note that the error bars in (b) are present but small ($< 1 \times 10^{-10}$ for all parameters). For both panels, the abscissa indicates the feature whose accuracy is being evaluated, and the ordinate depicts the average percent error across multiple voltammogram pairs. The bar shading pattern denotes the specific parameter being varied to generate the set of voltammograms evaluated; all other parameters are held at a constant value. All transient voltammograms used for this analysis were simulated at a scan rate of 10 mV s^{-1}, and the error bars represent one standard deviation from end-to-end.

Figure 4 illustrates that the parameters are estimated with lower accuracy for the "fundamental" set (maximum RMSE *ca*. 1×10^{-10} m^2 s^{-1} for D_O) and with greater accuracy for the "operational" case (maximum RMSE *ca*. 0.014 for the SOH). Overall, **Figure 4** demonstrates that the closed-

form steady-state expression for the current from a microelectrode may be used to accurately estimate the SOC and SOH of an electrolyte solution containing redox-active compounds, a finding consistent with previous *operando* studies.[9,12] However, the framework may not be as well suited to extract "fundamental" electrochemical parameters, as greater parameter estimation errors are exhibited. We suspect that the poorer estimation of the "fundamental" parameter set occurs because E_0 and d_O can be challenging to simultaneously and uniquely determine, since the mid-point potential is a function of both.[2] That said, other electrochemical and spectroscopic techniques (e.g., macroelectrode cyclic voltammograms,[1,2] diffusion ordered spectroscopy[64]) may also be employed to estimate or refine this parameter set.

The analogous procedure was also performed for the sequential electron transfer mechanism, with the results detailed in **Figure 5**; example data-model fits are also found in the SI (**Section S.3**). This analysis follows the same trend as **Figure 4**; specifically, the errors for the "fundamental" parameter estimation are significantly larger, with the maximum RMSE now approximately 5×10^{-10} m^2 s^{-1} (again for D_O). This larger error, as compared to the results in **Figure 4**, is tentatively attributed to the greater number of adjustable parameters—five in the sequential model compared to three in the single electron model—some of which are coupled. These errors may also be attributed to the different ways the closed-form and numerical models handle comproportionation, though this dissimilarity is likely not the primary factor—if it were, the errors would be notably larger when the diffusion coefficient ratios were varied. The total simulation time for all 77 optimizations also increased, with the maximum value now less than 50 s (**Figure 5b**). Analogously, the RMSE for the "operational" parameters is also small in **Figure 5**, never rising above 0.012 (again, for the SOH). Overall, **Figures 4** and **5** exhibit the same trends; the model appears well-suited to simultaneously estimate the SOC and SOH of an electrochemical

system, which is of utility for evaluating the dynamic behavior of electrochemical system in near-real time. In contrast, the current framework may not be as capable of accurately estimating fundamental parameters on its own.

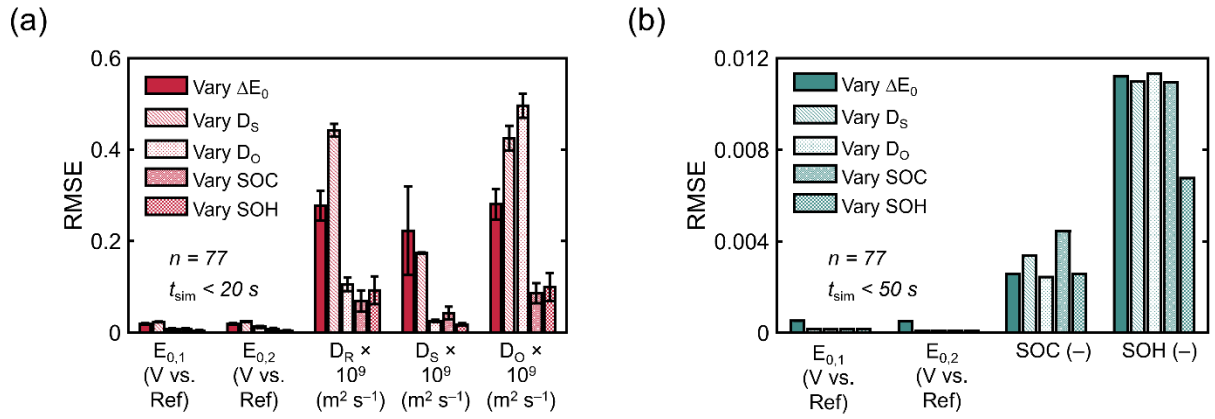

Figure 5. Error of feature estimation (n = 77 for each bar), evaluated in its entirety in less than 50 s, using the electrochemically reversible sequential electron transfer steady-state model. The two bar plots are ordered in a fashion analogous to **Figure 4**: (a) estimation of the "fundamental" parameter set and (b) estimation of the "operational" parameter set. Note that the error bars in (b) are present but small (< 1×10^{-10} for all parameters). All transient voltammograms used for this analysis were simulated at a scan rate of 10 mV s^{-1}, and the error bars represent one standard deviation from end-to-end.

3.4. Experimental validation

Experimental data was also evaluated alongside the numerical simulations to assess how well the framework can estimate characteristics of a representative electrolyte solution. To this end, a model single-electron-transfer compound, MEEPT, was studied. This compound has precedence as a positive charge-storage species for use in nonaqueous redox flow batteries and is chemically stable in both relevant oxidation states (R and O, per **Equation (1)**).[31,53] Though this approach evaluates a solution of nearly unchanging composition—as opposed to operating electrochemical systems—we anticipate our algorithm may also accurately probe electrochemical solutions of

dynamic composition if the data quality remains unchanged. It may not be trivial to obtain the desired quality of data from an operating electrochemical system, though initial studies have indicated this endeavor may be feasible.[31,37–39,65–67]

The measured values of the operational parameters—assumed to be ground truth for this study—were independently evaluated based on the masses of MEEPT and MEEPT–BF_4 added; Randles-Ševčik analyses and peak potential averaging were used to estimate the underlying "fundamental" parameters (E_0, D_R, and D_O) from macroelectrode voltammetry experiments conducted in solutions with SOCs of 0 and 1. Two additional solutions at intermediate SOC values (*ca.* ⅓ and ⅔) were evaluated to determine whether the protocol can estimate operational parameters. The estimated formal electrode potentials and the diffusion coefficient of MEEPT are similar to those reported in literature,[53,68] while the oxidized diffusion coefficient for MEEPT–BF_4 was not found; further details on the analysis are found in the SI (**Section S.5**), and the results of the automated SOC and SOH estimation are illustrated in **Figure 6**, where all 63 optimizations were performed in a total time of less than 25 s (**Figure 6b**).

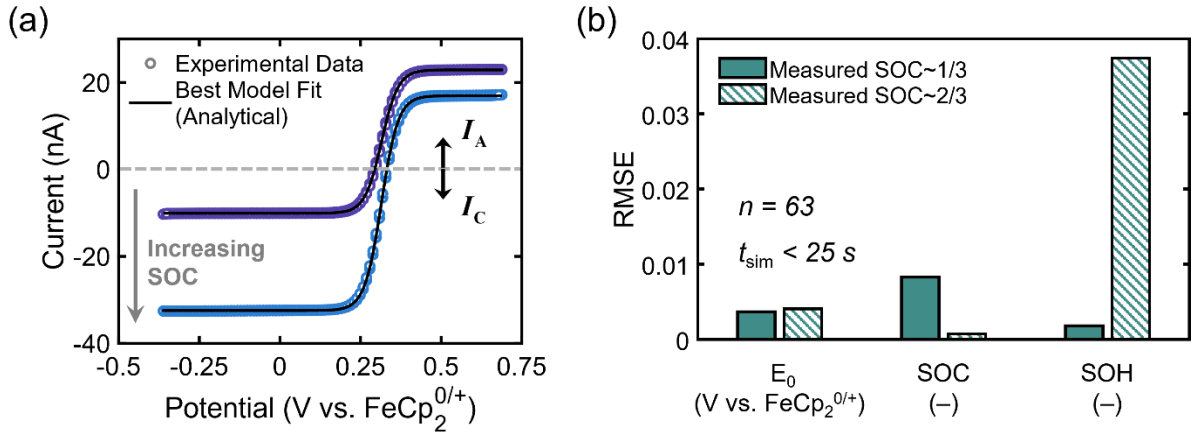

Figure 6. Evaluation of model accuracy using experimental microelectrode voltammograms of MEEPT and MEEPT–BF_4. Two solutions of SOCs of *ca*. ⅓ (top curve in panel (a)) and ⅔ (bottom curve) were studied. The ⅓ SOC solution contained *ca*. 9.39 mM MEEPT, 4.46 mM MEEPT–BF_4, and 0.53 M $TEABF_4$, while the ⅔ SOC solution contained *ca*. 7.33 mM MEEPT, 14.54 mM MEEPT–BF_4, and 0.55 M $TEABF_4$, both in acetonitrile. (a) Experimental data (dots) and the fitted model (solid line). Positive currents are oxidative (anodic), and negative currents are reductive (cathodic). (b) Error of the fundamental parameter set for sequential electron transfers (n = 63 for each bar), evaluated in its entirety in less than 25 s. All experimental voltammograms used for this analysis were acquired at a scan rate of 10 mV s^{-1}. The magnitude of every error bar—not visualized—is < 1×10^{-11} in all instances.

Figure 6a shows good agreement between the experimental and modeled responses at two different SOCs and two different total concentrations (i.e., two effective SOH values). Further, the errors of the estimated parameters (**Figure 6b**) are on the order of those found in **Figure 4b**, initially validating the results from the studies involving numerically simulated voltammograms. However, the largest error is now < 0.04, rather than the previously observed lower values of < 0.015. This increase in error may have multiple causes, including inaccurate estimations in the fundamental parameters—themselves estimated from experimental data, rather than directly set by the user—and other experimental errors (e.g., measurement precision). These factors may result in minor differences in accuracy between experimental and synthetic data, but the errors remain within the same order of magnitude. Overall, the experiments performed in this work evince that the microelectrode models employed can estimate operational parameters almost as accurately as

was predicted using synthetic data. This encouraging finding suggests that component concentrations in electrolyte solutions may be rapidly and accurately estimated in an automated fashion using microelectrode voltammetry and that, with a suitable configuration, this protocol may be able to estimate features of interest within operating electrochemical devices.[31] As such, these models are being further explored, both to capture a wider range of redox reaction conditions—such as combined migration-diffusion transport—and to complement other characterization techniques (e.g., macroelectrode voltammetry, UV-Vis spectroscopy) to augment (perhaps *in situ* or *operando*) electrochemical analyses of electrolyte solutions.[40]

4. Conclusions

Microelectrode voltammetry is a powerful approach to studying the behavior of electrolyte solutions and may be leveraged to evaluate useful features within electrochemical cells. In this study, we used oblate spheroidal coordinates to model the voltammetric responses of disk microelectrodes by presenting two frameworks that may enable users to derive closed-form steady-state expressions for multiple electron transfer mechanisms (here, single and sequential electron transfers) with greater ease. The coordinate system was also leveraged to simplify the construction of a finite-difference simulator, useful for scenarios under which analytical solutions only approximate microelectrode behavior. The in-house numerical simulator was successfully validated against COMSOL®, a commercial multiphysics simulator. The closed-form expressions, in turn, were shown to be capable of accurately estimating parameters from transient voltammograms—both numerically simulated and experimentally obtained—validating the predictive power of this approach.

Oblate spheroidal coordinates are an amenable coordinate system for electrochemical systems containing a disk—or more generally an oblate hemispheroid—electrode surrounded by an insulating surface;[43] herein, we verify the utility of this coordinate system in simulating microelectrode voltammograms of electrolyte solutions containing redox-active compounds at low concentrations. This framework may be extended to construct simulators that capture more complex physical phenomena (e.g., simultaneous analyte migration and diffusion) encountered in electrochemical systems. The results from this framework may also be paired with other experiments to infer more information about the solution being studied than would be possible from any single technique alone.

Our in-house automated parameter estimation routine can also be extended to accelerate additional voltammetry data analyses previously conducted manually. For example, exact or approximate closed-form solutions may be leveraged to estimate the SOC and SOH of electrolyte solutions in electrochemical devices (e.g., redox flow batteries) in an automated fashion and in near-real time, given a sufficient (currently unquantified) data quality.[9,31] In sum, future work will aim to expand the capabilities and utility of this modeling framework to more comprehensively analyze the behavior of electrolyte solutions within practical electrochemical embodiments.

5. Acknowledgments

This work was supported by the National Science Foundation (NSF) under Award Number 1805566. B.J.N. and K.M.T. also gratefully acknowledge the NSF Graduate Research Fellowship Program under Grant Numbers 1122374 and 2141064. Any opinion, findings, and conclusions or recommendations expressed in this material are those of the authors and do not necessarily reflect

the views of the NSF. This work was also partially supported as part of the Joint Center for Energy Storage Research, an Energy Innovation Hub funded by the U.S. Department of Energy, Office of Science, Basic Energy Sciences. A.M.F., Jr. also gratefully acknowledges financial support provided by the MIT MathWorks Engineering Fellowship. We thank the late Professor Susan Odom, Professor Aman Kaur, and the Odom Research Group for synthesizing, purifying and shipping the oxidized form of the phenothiazine derivative used in this work.

6. CRediT Authorship Statement

A.M.F., Jr. performed the conceptualization, methodology, software, validation, formal analysis, investigation, data curation, writing−original draft, writing−review and editing, and visualization. B.J.N. performed the conceptualization, methodology, validation, investigation, writing−original draft, writing−review and editing, and visualization. K.M.T. performed the methodology, software, validation, investigation, writing−original draft, writing−review and editing, and visualization. Y.-M.C. performed the funding acquisition and resources. F.R.B. performed the conceptualization, funding acquisition, project administration, resources, supervision, visualization, writing−original draft, writing−review and editing.

7. Competing Interests and Funding

The authors declare no competing financial interest.

6. Glossary

Latin variables

A_e	Surface area of the working electrode (m^2)
a_1	Constant of integration (–)
a_2	Constant of integration (–)
b_1	Constant of integration (–)
b_2	Constant of integration (–)
b_3	Constant of integration (–)
b_4	Constant of integration (–)
C_j	Concentration of species j (mol m^{-3})
$C_{j,\infty}$	Bulk or initial concentration of j (mol m^{-3})
$C_{j,S'}$	Concentration of species j on the surface of the electrode (mol m^{-3})
$C_{\text{total},\infty}$	Total bulk concentration of all species (mol m^{-3})
c_j	Dimensionless concentration of species j (–)
$c_{j,\infty}$	Dimensionless bulk or initial concentration of j (–)
D_j	Diffusion coefficient of species j (m^2 s^{-1})
dA	Generic areal element (m^2)
d_j	Ratio of diffusion coefficients $D_j D_R^{-1}$ (–)
E	Applied electrode potential (V vs. reference redox event)
E_0	Formal redox potential for a species of interest (V vs. reference redox event)
$E_{0,1}$	Formal redox potential for the more reductive electron transfer in a sequential mechanism (V vs. reference redox event)
$E_{0,2}$	Formal redox potential for the more oxidative electron transfer in a sequential mechanism (V vs. reference redox event)
$E_{0,\text{avg}}$	Average of the reductive and oxidative redox potentials of a sequential electron transfer mechanism (V vs. reference redox event)
F	Faraday constant (96485 C mol^{-1})
f_j	Fraction of species j in the bulk (–)
g	Indexing counter (–)
I	Current (A)
$\boldsymbol{I}(\boldsymbol{\theta})$	Vector of modeled currents (A)
I_1	Current generated by the more reductive electron transfer in a sequential mechanism (A)

I_2	Current generated by the more oxidative electron transfer in a sequential mechanism (A)
I_a	Anodic current symbol (A)
I_c	Cathodic current symbol (A)
$\mathbf{I_{obs}}$	Vector of measured currents (A)
i	Indexing counter (–)
i_{curr}	Current density (A m^{-2})
iR	Ohmic potential distortion (V)
$\mathbf{J}_i$	Flux vector of species i (mol m^{-2} s^{-1})
j	Indexing counter (–)
K_0	Dimensionless heterogeneous rate constant (–)
$K_{0,1}$	Dimensionless heterogeneous rate constant for the more reductive electron transfer in a sequential mechanism (–)
$K_{0,2}$	Dimensionless heterogeneous rate constant for the more oxidative electron transfer in a sequential mechanism (–)
k	Indexing counter (–)
k_o	Heterogeneous rate constant (m s^{-1})
l	Indexing counter (–)
m_T	Mass transfer coefficient (m s^{-1})
N_t	Number of total trials evaluated to calculate errors (–)
n	Number of optimizations performed (–)
$\mathbf{n}$	Normal vector in the radial or axial direction (m)
n_e	Number of electrons transferred (–)
P	A function used in the separation of variables approach only dependent on η (–)
Q	A function used in the separation of variables approach only dependent on ξ (–)
q	Indexing counter (–)
R_G	Universal gas constant (8.314 J mol^{-1} K^{-1})
R_i	Volumetric reaction rate of species i (mol m^{-3} s^{-1})
RMSE_i	Root mean squared error of parameter i (varied units)
r	Radial spatial coordinate (m)
r_e	Working electrode radius (m)
SOC	State-of-charge (–)
SOH	State-of-health (–)
T	Absolute temperature (K)
t	Time (s)
t_{sim}	Total time to conduct η regressions on synthetic or experimental data (s)
$\mathbf{u}$	Velocity vector (m s^{-1})
z	Axial spatial coordinate (m)

Greek variables

α_c	Cathodic transfer coefficient (–)
$\alpha_{c,1}$	Cathodic transfer coefficient for the more reductive electron transfer in a sequential mechanism (–)
$\alpha_{c,2}$	Cathodic transfer coefficient for the more oxidative electron transfer in a sequential mechanism (–)
ΔE_0	Difference in redox potentials in a sequential electron transfer mechanism (V)
δ_{BL}	Non-dimensional boundary layer length (–)
η	Oblate spheroidal coordinate perpendicular to the microelectrode surface (–)
$\boldsymbol{\theta}$	Generic vector of electrochemical and transport parameters (multiple units)
$\boldsymbol{\theta}_{\mathbf{best}}$	Vector of best-fit electrochemical and transport parameters (multiple units)
$\theta_{i,k,\mathrm{guess}}$	Value of the estimated parameter i of the k^{th} trial (varied units)
$\boldsymbol{\theta}_{\boldsymbol{k},\mathbf{guess}}$	Vector of estimated parameters for the k^{th} trial (multiple units)
$\theta_{i,k,\mathrm{true}}$	Value of the true parameter i of the k^{th} trial (varied units)
$\boldsymbol{\theta}_{\boldsymbol{k},\mathbf{true}}$	Vector of true parameters for the k^{th} trial (multiple units)
ξ	Oblate spheroidal coordinate parallel to the microelectrode surface (–)
τ	Dimensionless time (–)
υ_i	Stoichiometric coefficient of species i (–)
ϕ_l	Electrolyte potential or ohmic drop (V)
φ	Dimensional overpotential (V)
φ_1	Dimensional overpotential for the more reductive electron transfer in a sequential mechanism (V)
φ_2	Dimensional overpotential for the more oxidative electron transfer in a sequential mechanism (V)

Latin symbols

O	Oxidized form of a redox couple
R	Reduced form of a redox couple
S	Semi-oxidized, or semi-reduced, form of a redox couple
S'	A generic surface

9. References

(1) Compton, R. G.; Banks, C. E. *Understanding Voltammetry*, 2nd ed.; Imperial College Press: London, 2011.

(2) Bard, A. J.; Faulkner, L. R. *Electrochemical Methods: Fundamentals and Applications*, 2nd ed.; John Wiley & Sons. Inc.: New York, 2001.

(3) *Microelectrodes: Theory and Applications*; Montenegro, M. I., Queirós, M. A., Daschbach, J. L., Eds.; Kluwer Academic Publishers: Dordrecht, 1991.

(4) Mirčeski, V.; Komorsky-Lovrić, Š.; Lovrić, M. *Square-Wave Voltammetry: Theory and Application*; Springer-Verlag Berlin Heidelberg: Berlin/Heidelberg, 2007.

(5) Kwabi, D. G.; Lin, K.; Ji, Y.; Kerr, E. F.; Goulet, M.-A.; De Porcellinis, D.; Tabor, D. P.; Pollack, D. A.; Aspuru-Guzik, A.; Gordon, R. G.; Aziz, M. J. Alkaline Quinone Flow Battery with Long Lifetime at pH 12. *Joule* **2018**, *2* (9), 1894–1906. https://doi.org/10.1016/j.joule.2018.07.005.

(6) Helfrick, J. C.; Bottomley, L. A. Cyclic Square Wave Voltammetry of Single and Consecutive Reversible Electron Transfer Reactions. *Anal. Chem.* **2009**, *81* (21), 9041–9047. https://doi.org/10.1021/ac9016874.

(7) Bieniasz, L. K. A New Theory of Potential Step Chronoamperometry at a Microdisk Electrode: Complete Explicit Semi-Analytical Formulae for the Faradaic Current Density and the Faradaic Current. *Electrochimica Acta* **2016**, *199*, 1–11. https://doi.org/10.1016/j.electacta.2016.03.053.

(8) Jennings, J. R.; Huang, Q.; Wang, Q. Kinetics of Li_xFePO_4 Lithiation/Delithiation by Ferrocene-Based Redox Mediators: An Electrochemical Approach. *J. Phys. Chem. C* **2015**, *119*, 17522–17528. https://doi.org/10.1021/acs.jpcc.5b03561.

(9) Kowalski, J. A.; Fenton Jr., A. M.; Neyhouse, B. J.; Brushett, F. R. A Method for Evaluating Soluble Redox Couple Stability Using Microelectrode Voltammetry. *J. Electrochem. Soc.* **2020**, *167* (16), 160513. https://doi.org/10.1149/1945-7111/abb7e9.

(10) Komorsky-Lovrić, Š.; Vukašinović, N.; Penovski, R. Voltammetric Determination of Microparticles of Some Local Anesthetics and Antithusics Immobilized on the Graphite Electrode. *Electroanalysis* **2003**, *15* (5–6), 544–547. https://doi.org/10.1002/elan.200390067.

(11) Compton, R. G.; Laborda, E.; Ward, K. R. *Understanding Voltammetry: Simulation of Electrode Processes*; Imperial College Press: London, 2014.

(12) Stolze, C.; Meurer, J. P.; Hager, M. D.; Schubert, U. S. An Amperometric, Temperature-Independent, and Calibration-Free Method for the Real-Time State-of-Charge Monitoring of Redox Flow Battery Electrolytes. *Chem. Mater.* **2019**, *31* (15), 5363–5369. https://doi.org/10.1021/acs.chemmater.9b02376.

(13) Mann, M. A.; Helfrick, Jr., J. C.; Bottomley, L. A. Diagnostic Criteria for the Characterization of Quasireversible Electron Transfer Reactions by Cyclic Square Wave Voltammetry. *Anal. Chem.* **2014**, *86*, 8183–8191. https://doi.org/10.1021/ac501550j.

(14) Bond, A. M.; Oldham, K. B.; Zoski, C. G. Theory of Electrochemical Processes at an Inlaid Disc Microelectrode under Steady-State Conditions. *J. Electroanal. Chem.* **1988**, *245* (1–2), 71–104. https://doi.org/10.1016/0022-0728(88)80060-3.

(15) Oldham, K. B.; Myland, J. C. Modelling Cyclic Voltammetry without Digital Simulation. *Electrochimica Acta* **2011**, *56*, 10612–10625. https://doi.org/10.1016/j.electacta.2011.05.044.

(16) Lavacchi, A.; Bardi, U.; Borri, C.; Caporali, S.; Fossati, A.; Perissi, I. Cyclic Voltammetry Simulation at Microelectrode Arrays with COMSOL Multiphysics®. *J. Appl. Electrochem.* **2009**, *39*, 2159. https://doi.org/10.1007/s10800-009-9797-2.
(17) EC-Lab® Software User's Manual - Version 10.38, 2014.
(18) Myland, J. C.; Oldham, K. B. Modelling Diffusion to a Disk Electrode by Fully Explicit Simulation. *J. Electroanal. Chem.* **2005**, *576* (2), 353–362. https://doi.org/10.1016/j.jelechem.2004.10.031.
(19) Fenton Jr., A. M.; Brushett, F. R. Using Voltammetry Augmented with Physics-Based Modeling and Bayesian Hypothesis Testing to Identify Analytes in Electrolyte Solutions. *J. Electroanal. Chem.* **2022**, *904*, 115751. https://doi.org/10.1016/j.jelechem.2021.115751.
(20) Klymenko, O. V.; Svir, I.; Oleinick, A.; Amatore, C. A Novel Approach to the Simulation of Electrochemical Mechanisms Involving Acute Reaction Fronts at Disk and Band Microelectrodes. *ChemPhysChem* **2012**, *13* (3), 845–859. https://doi.org/10.1002/cphc.201100825.
(21) Lavagnini, I.; Pastore, P.; Magno, F.; Amatore, C. A. Performance of a Numerical Method Based on the Hopscotch Algorithm and on an Oblate Spheroidal Space Coordinate-Expanding Time Grid for Simulation of Voltammetric Curves at an Inlaid Disk Microelectrode. *J. Electroanal. Chem. Interfacial Electrochem.* **1991**, *316* (1), 37–47. https://doi.org/10.1016/0022-0728(91)87034-2.
(22) Oleinick, A.; Svir, I.; Amatore, C. A Few Key Theoretical Issues of Importance in Modern Molecular Electrochemistry. *Curr. Opin. Electrochem.* **2019**, *13*, 33–39. https://doi.org/10.1016/j.coelec.2018.10.008.
(23) Amatore, C. A.; Fosset, B. Space Variables Well Fitted for the Study of Steady State and Near-Steady-State Diffusion at a Microdisk. *J. Electroanal. Chem.* **1992**, *328* (1), 21–32. https://doi.org/10.1016/0022-0728(92)80167-3.
(24) Amatore, C.; Pebay, C.; Thouin, L.; Wang, A.; Warkocz, J.-S. Difference between Ultramicroelectrodes and Microelectrodes: Influence of Natural Convection. *Anal. Chem.* **2010**, *82* (16), 6933–6939. https://doi.org/10.1021/ac101210r.
(25) Michael, A. C.; Wightman, R. M.; Amatore, C. A. Microdisk Electrodes: Part I. Digital Simulation with a Conformal Map. *J. Electroanal. Chem. Interfacial Electrochem.* **1989**, *267* (1), 33–45. https://doi.org/10.1016/0022-0728(89)80235-9.
(26) Lin, K.; Chen, Q.; Gerhardt, M. R.; Tong, L.; Kim, S. B.; Eisenach, L.; Valle, A. W.; Hardee, D.; Gordon, R. G.; Aziz, M. J.; Marshak, M. P. Alkaline Quinone Flow Battery. *Science* **2015**, *349* (6255), 1529–1532. https://doi.org/10.1126/science.aab3033.
(27) Kowalski, J. A.; Casselman, M. D.; Kaur, A. P.; Milshtein, J. D.; Elliott, C. F.; Modekrutti, S.; Attanayake, N. H.; Zhang, N.; Parkin, S. R.; Risko, C.; Brushett, F. R.; Odom, S. A. A Stable Two-Electron-Donating Phenothiazine for Application in Nonaqueous Redox Flow Batteries. *J. Mater. Chem. A* **2017**, *5*, 24371–24379. https://doi.org/10.1039/C7TA05883G.
(28) Bond, A. M. Past, Present and Future Contributions of Microelectrodes to Analytical Studies Employing Voltammetric Detection: A Review. *The Analyst* **1994**, *119* (11), 1–21. https://doi.org/10.1039/AN994190001R.
(29) Gunasekara, I.; Mukerjee, S.; Plichta, E. J.; Hendrickson, M. A.; Abraham, K. M. Microelectrode Diagnostics of Lithium-Air Batteries. *J. Electrochem. Soc.* **2014**, *161* (3), A381–A392. https://doi.org/10.1149/2.073403jes.

(30) Attanayake, N. H.; Kowalski, J. A.; Greco, K. V.; Casselman, M. D.; Milshtein, J. D.; Chapman, S. J.; Brushett, F. R.; Odom, S. A. Tailoring Two-Electron-Donating Phenothiazines To Enable High-Concentration Redox Electrolytes for Use in Nonaqueous Redox Flow Batteries. *Chem. Mater.* **2019**, *31* (12), 4353–4363. https://doi.org/10.1021/acs.chemmater.8b04770.
(31) Neyhouse, B. J.; Tenny, K. M.; Chiang, Y.-M.; Brushett, F. R. Microelectrode-Based Sensor for Measuring Operando Active Species Concentrations in Redox Flow Cells. *ACS Appl. Energy Mater.* **2021**, *4* (12), 13830–13840. https://doi.org/10.1021/acsaem.1c02580.
(32) Oldham, K. B.; Myland, J. C.; Zoski, C. G.; Bond, A. M. Kinetic Parameters from Steady-State Voltammograms at Microdisc Electrodes. *J. Electroanal. Chem. Interfacial Electrochem.* **1989**, *270*, 79–101. https://doi.org/10.1016/0022-0728(89)85029-6.
(33) Limon-Petersen, J. G.; Dickinson, E. J. F.; Belding, S. R.; Rees, N. V.; Compton, R. G. Cyclic Voltammetry in Weakly Supported Media: The Reduction of the Cobaltocenium Cation in Acetonitrile – Comparison between Theory and Experiment. *J. Electroanal. Chem.* **2010**, *650* (1), 135–142. https://doi.org/10.1016/j.jelechem.2010.08.011.
(34) Saito, Y. A Theoretical Study on the Diffusion Current at the Stationary Electrodes of Circular and Narrow Band Types. *Rev. Polarogr.* **1968**, *15* (6), 177–187. https://doi.org/10.5189/revpolarography.15.177.
(35) Nolte, O.; Volodin, I. A.; Stolze, C.; Hager, M. D.; Schubert, U. S. Trust Is Good, Control Is Better: A Review on Monitoring and Characterization Techniques for Flow Battery Electrolytes. *Mater. Horiz.* **2021**, *8* (7), 1866–1925. https://doi.org/10.1039/D0MH01632B.
(36) Pence, M. A.; Rodríguez, O.; Lukhanin, N. G.; Schroeder, C. M.; Rodríguez-López, J. Automated Measurement of Electrogenerated Redox Species Degradation Using Multiplexed Interdigitated Electrode Arrays. *ACS Meas. Sci. Au* **2023**, *3* (1), 62–72. https://doi.org/10.1021/acsmeasuresciau.2c00054.
(37) Volodin, I. A.; Stolze, C.; Nolte, O.; Rohland, P.; Hager, M. D.; Schubert, U. S. State and Prospects of Unbalanced, Compositionally Symmetric Flow Battery Cycling and Steady-State Amperometry Techniques for Electrolyte Stability Assessment: The Case of Methyl Viologen. *ACS Appl. Energy Mater.* **2023**, *6* (1), 302–316. https://doi.org/10.1021/acsaem.2c02959.
(38) Stolze, C.; Rohland, P.; Zub, K.; Nolte, O.; Hager, M. D.; Schubert, U. S. A Low-Cost Amperometric Sensor for the Combined State-of-Charge, Capacity, and State-of-Health Monitoring of Redox Flow Battery Electrolytes. *Energy Convers. Manag. X* **2022**, *14*, 100188. https://doi.org/10.1016/j.ecmx.2022.100188.
(39) Fenton, A. M. Jr.; Ashraf Gandomi, Y.; Mallia, C. T.; Neyhouse, B. J.; Kpeglo, M. A.; Exson, W. E.; Wan, C. T.-C.; Brushett, F. R. Toward a Mechanically Rechargeable Solid Fuel Flow Battery Based on Earth-Abundant Materials. *ACS Omega* **2022**, *7* (44), 40540–40547. https://doi.org/10.1021/acsomega.2c05798.
(40) Fenton Jr., A. M.; Brushett, F. R. Leveraging Graphical Models to Enhance *in situ* Analyte Identification *via* Multiple Voltammetric Techniques. *J. Electroanal. Chem.* **2023**, *936*, 117299. https://doi.org/10.1016/j.jelechem.2023.117299.
(41) Neyhouse, B. J.; Fenton Jr., A. M.; Brushett, F. R. Too Much of a Good Thing? Assessing Performance Tradeoffs of Two-Electron Compounds for Redox Flow Batteries. *J. Electrochem. Soc.* **2021**, *168* (5), 050501. https://doi.org/10.1149/1945-7111/abeea3.

(42) Birke, R. L. Steady State Concentrations and Currents on an Oblate Spheroid Microelectrode. *J. Electroanal. Chem.* **1989**, *274* (1–2), 297–304. https://doi.org/10.1016/0022-0728(89)87052-4.
(43) Qian, W.; Jin, B.; Diao, G.; Zhang, Z.; Shi, H. Application of a Finite Analytic Numerical Method. Part 2. Digital Simulation of Charge Transfer to an Oblate Hemispheroid Microelectrode and Experiment Verification. *J. Electroanal. Chem.* **1996**, *414*, 1–10. https://doi.org/10.1016/0022-0728(96)04647-5.
(44) Molina, A.; Gonzalez, J.; Barnes, E. O.; Compton, R. G. Simple Analytical Equations for the Current-Potential Curves at Microelectrodes: A Universal Approach. *J. Phys. Chem. C* **2014**, *118* (1), 346–356. https://doi.org/10.1021/jp409167m.
(45) Molina, A.; González, J.; Laborda, E.; Compton, R. G. Analytical Solutions for Fast and Straightforward Study of the Effect of the Electrode Geometry in Transient and Steady State Voltammetries: Single- and Multi-Electron Transfers, Coupled Chemical Reactions and Electrode Kinetics. *J. Electroanal. Chem.* **2015**, *756*, 1–21. https://doi.org/10.1016/j.jelechem.2015.07.030.
(46) Newman, J. Resistance for Flow of Current to a Disk. *J. Electrochem. Soc.* **1966**, *113* (5), 501–502. https://doi.org/10.1149/1.2424003.
(47) Oldham, K. B. Steady-State Concentrations and Fluxes in the Vicinity of a Reversible Inlaid Disc Microelectrode. *J. Electroanal. Chem.* **1989**, *260*, 461–467. https://doi.org/10.1016/0022-0728(89)87162-1.
(48) Jin, B.; Qian, W.; Zhang, Z.; Shi, H. Application of the Finite Analytical Numerical Method. Part 3: Digital Simulation of Charge Transfer to a Micro-Ring Electrode Interface. *J. Electroanal. Chem.* **1996**, *417* (1–2), 45–51. https://doi.org/10.1016/S0022-0728(96)04753-5.
(49) Rongfeng, Z.; Evans, D. H. The Current for a Two-Electron Reaction Is Not Necessarily Twice That of a One-Electron Reaction. *J. Electroanal. Chem.* **1995**, *385* (2), 201–207. https://doi.org/10.1016/0022-0728(94)03783-Y.
(50) Mistry, A.; Verma, A.; Sripad, S.; Ciez, R.; Sulzer, V.; Brosa Planella, F.; Timms, R.; Zhang, Y.; Kurchin, R.; Dechent, P.; Li, W.; Greenbank, S.; Ahmad, Z.; Krishnamurthy, D.; Fenton, A. M.; Tenny, K.; Patel, P.; Juarez Robles, D.; Gasper, P.; Colclasure, A.; Baskin, A.; Scown, C. D.; Subramanian, V. R.; Khoo, E.; Allu, S.; Howey, D.; DeCaluwe, S.; Roberts, S. A.; Viswanathan, V. A Minimal Information Set To Enable Verifiable Theoretical Battery Research. *ACS Energy Lett.* **2021**, *6* (11), 3831–3835. https://doi.org/10.1021/acsenergylett.1c01710.
(51) *Voltammetry at a Microdisk Electrode*. COMSOL®. https://www.comsol.com/model/voltammetry-at-a-microdisk-electrode-12877 (accessed 2022-04-03).
(52) Electrochemistry Module User's Guide, COMSOL®. 2017.
(53) Milshtein, J. D.; Kaur, A. P.; Casselman, M. D.; Kowalski, J. A.; Modekrutti, S.; Zhang, P. L.; Attanayake, N. H.; Elliott, C. F.; Parkin, S. R.; Risko, C.; Brushett, F. R.; Odom, S. A. High Current Density, Long Duration Cycling of Soluble Organic Active Species for Non-Aqueous Redox Flow Batteries. *Energy Environ. Sci.* **2016**, *9* (11), 3531–3543. https://doi.org/10.1039/c6ee02027e.

(54) Kaur, A. P.; Harris, O. C.; Attanayake, N. H.; Liang, Z.; Parkin, S. R.; Tang, M. H.; Odom, S. A. Quantifying Environmental Effects on the Solution and Solid-State Stability of a Phenothiazine Radical Cation. *Chem. Mater.* **2020**, *32* (7), 3007–3017. https://doi.org/10.1021/acs.chemmater.9b05345.
(55) Gagné, R. R.; Koval, C. A.; Lisensky, G. C. Ferrocene as an Internal Standard for Electrochemical Measurements. *Inorg. Chem.* **1980**, *19*, 2855–2857. https://doi.org/10.1021/ic50211a080.
(56) Frkonja-Kuczin, A.; Alicea-Salas, J. Y.; Arroyo-Currás, N.; Boika, A. Hot-SWV: Square Wave Voltammetry with Hot Microelectrodes. *Anal. Chem.* **2020**, *92*, 8852–8858. https://doi.org/10.1021/acs.analchem.0c00427.
(57) Zotti, G.; Schiavon, G.; Zecchin, S.; Favretto, D. Dioxygen-Decomposition of Ferrocenium Molecules in Acetonitrile: The Nature of the Electrode-Fouling Films during Ferrocene Electrochemistry. *J. Electroanal. Chem.* **1998**, *456* (1), 217–221. https://doi.org/10.1016/S0022-0728(98)00279-4.
(58) EC-Lab® Software: Techniques and Applications - Version 10.38, 2014.
(59) Mirkin, M. V.; Bard, A. J. Simple Analysis of Quasi-Reversible Steady-State Voltammograms. *Anal. Chem.* **1992**, *64* (19), 2293–2302. https://doi.org/10.1021/ac00043a020.
(60) Oldham, K. B.; Zoski, C. G. Comparison of Voltammetric Steady States at Hemispherical and Disc Microelectrodes. *J. Electroanal. Chem. Interfacial Electrochem.* **1988**, *256* (1), 11–19. https://doi.org/10.1016/0022-0728(88)85002-2.
(61) Bond, A. M.; Mahon, P. J. Linear and Non-Linear Analysis Using the Oldham–Zoski Steady-State Equation for Determining Heterogeneous Electrode Kinetics at Microdisk Electrodes and Digital Simulation of the Microdisk Geometry with the Fast Quasi-Explicit Finite Difference Method. *J. Electroanal. Chem.* **1997**, *439* (1), 37–53. https://doi.org/10.1016/S0022-0728(97)00370-7.
(62) Quan, M.; Sanchez, D.; Wasylkiw, M. F.; Smith, D. K. Voltammetry of Quinones in Unbuffered Aqueous Solution: Reassessing the Roles of Proton Transfer and Hydrogen Bonding in the Aqueous Electrochemistry of Quinones. *J. Am. Chem. Soc.* **2007**, *129* (8), 12847–12856. https://doi.org/10.1021/ja0743083.
(63) Goulet, M.-A.; Aziz, M. J. Flow Battery Molecular Reactant Stability Determined by Symmetric Cell Cycling Methods. *J. Electrochem. Soc.* **2018**, *165* (7), A1466–A1477. https://doi.org/10.1149/2.0891807jes.
(64) Shkrob, I. A.; Robertson, L. A.; Yu, Z.; Assary, R. S.; Cheng, L.; Zhang, L.; Sarnello, E.; Liu, X.; Li, T.; Kaur, A. P.; Suduwella, T. M.; Odom, S. A.; Wang, Y.; Ewoldt, R. H.; Farag, H. M.; Z, Y. Crowded Electrolytes Containing Redoxmers in Different States of Charge: Solution Structure, Properties, and Fundamental Limits on Energy Density. *J. Mol. Liq.* **2021**, *334*, 116533. https://doi.org/10.1016/j.molliq.2021.116533.
(65) Jacquemond, R. R.; Geveling, R.; Forner-Cuenca, A.; Nijmeijer, K. On the Characterization of Membrane Transport Phenomena and Ion Exchange Capacity for Non-Aqueous Redox Flow Batteries. *J. Electrochem. Soc.* **2022**, *169* (8), 080528. https://doi.org/10.1149/1945-7111/ac8623.
(66) Kim, D.; Sanford, M. S.; Vaid, T. P.; McNeil, A. J. A Nonaqueous Redox-Matched Flow Battery with Charge Storage in Insoluble Polymer Beads. *Chem. – Eur. J.* **2022**, *28* (25), e202200149. https://doi.org/10.1002/chem.202200149.

(67) Neyhouse, B.; Darling, R.; Saraidaridis, J.; Brushett, F. A Method for Quantifying Crossover in Redox Flow Cells through Compositionally Unbalanced Symmetric Cell Cycling. ChemRxiv March 17, 2023. https://doi.org/10.26434/chemrxiv-2023-nv20t.
(68) Attanayake, N. H.; Suduwella, T. M.; Yan, Y.; Kaur, A. P.; Liang, Z.; Sanford, M. S.; Odom, S. A. Comparative Study of Organic Radical Cation Stability and Coulombic Efficiency for Nonaqueous Redox Flow Battery Applications. *J. Phys. Chem. C* **2021**, *125* (26), 14170–14179. https://doi.org/10.1021/acs.jpcc.1c00686.